UNDERSTANDING SUBSURFACE INTEGRITY IN MACHINING OF CELLULAR SOLIDS

A Thesis
Submitted to
The Academic Faculty of
Georgia Institute of Technology

by

Haipeng Qiao

In Partial Fulfillment of the
Requirements for the Degree
of
Master of Science
in Mechanical Engineering

August 2017
Georgia Institute of Technology
Atlanta, Georgia

UNDERSTANDING SUBSURFACE INTEGRITY IN MACHINING OF CELLULAR SOLIDS

by

Haipeng Qiao

Approved by

Dr. Christopher Saldana, Advisor
School of Mechanical Engineering
Georgia Institute of Technology

Dr. Thomas Kurfess
School of Mechanical Engineering
Georgia Institute of Technology

Dr. Tejas Murthy
Department of Civil Engineering
Indian Institute of Science

Date Approved: July 26th, 2017

ACKNOWLEDGEMENTS

I would like to thank my thesis advisor, Dr. Christopher Saldana for his kind support, guidance and encouragement throughout the years of my graduate studies. I would also like to thank my thesis committee members, Dr. Thomas Kurfess and Dr. Tejas Murthy, for their wisdom and support towards the improvement of this work.

I would like to express my gratitude to my colleagues throughout the years: Zhiyu Wang, Saurabh Basu, John Miers, Maxwell Praniewicz and Austin Jiang. Zhiyu's expertise in Particle Image Velocimetry has been helpful in the development of Digital Volume Correlation. Discussion with Saurabh and John on Computed Tomography has enabled me to understand the technique comprehensively. Assistance from Max and Austin has facilitated my experimental work on metal cutting and *in situ* compression tests. I sincerely thank them for their help and assistance.

I would like to express my deepest gratitude towards my parents for their continuous support and belief in me.

Table of Contents

LIST OF TABLES

LIST OF FIGURES

SUMMARY

Thermomechanical loading during surface severe plastic deformation in machining is marked by the generation of high and graded strains, strain rates and temperatures in bulk materials. The present study examined the surface integrity of cellular solids processed by machining-based processing at full volume using x-ray micro-computed tomography. The structural parameters of the strut-pore network were characterized as a function of controllable parameters of cutting speed, feed rate and depth of cut. The resulting surfaces were shown to be comprised of density gradients directly controlled by the processing parameters employed. A series of *in situ* compressive loading experiments was conducted to evaluate the effect of the structural gradation on mechanical response and showed enhanced plateau stress levels at low strains for the graded surfaces. Direct measurements of incremental strain using digital volume correlation identified the role of the gradation in arresting deformation at low strains. Implications of these results for using surface deformation processing in achieving specific properties by functional gradation were briefly discussed.

CHAPTER 1. INTRODUCTION

1.1. Motivation

Low density cellular metals, or metal foams, are an important class of complex materials, with unique thermal, electrical acoustic, and mechanical properties [1, 2]. They have been adopted in a wide range of specialized products and processes. For automotive and aerospace applications, these materials provide capability for structural lightweighting and enhanced impact absorption [2]. In biomedical applications, cellular metal foams are next generation systems for engineered implants due to their enhanced biomechanical and bio-integration performance [3]. In the chemical and energy industries, these materials are useful for high temperature filtration applications [2]. Depending on the specific application of interest, functional response (e.g., strength, stiffness, transport) of the cellular solid is determined by geometric characteristics of the network of struts and nodes and their distribution throughout the solid.

Attention has been paid to studying the use of structural gradients at the surface of these materials, to realize the attendant benefits of functional gradation of structure and properties that are often observed in naturally-occurring biological systems. In this regard, functional gradation of density of cellular solids has garnered significant interest and has been shown to yield rising plateau stresses [4], facilitate double plateau stresses [5], enhance energy absorption [6], reduce weight in yield-limited systems designs [7] and enhance heat transfer [8]. The source of the enhanced load bearing capacity in

quasi-static and dynamic loading conditions has been explained by the progression in plastic accommodation from low density (e.g., large pore) regions at low strains to regions of high density (e.g., small pore) at higher strains. For continuously graded foams, this results in a steadily rising plateau stress [4] as deformation transmits through the differently-graded regions. In contrast, foams with binary-type gradation (e.g., high/low) in structure [5] exhibit double plateau stress response. In this regard, Hangai et al. [5] has utilized computed tomography and *ex situ* loading experiments to directly show that failure in compressive loading of such a graded aluminum foam initiated in regions of high porosity during the first plateau stress level, followed by deformation in regions of low porosity during the second plateau event.

Gradation of cellular solids has been achieved by a number of processing routes, mostly by either top-down routes using electrochemical processing and chemical dissolution or by specialized bottom-up routes based on powder compaction, pulsed sintering or direct energy deposition [9-12]. While use of precursors and electrochemical processing has been useful in achieving a high degree of control in generating functionally graded structures, their use in high rate production processes or large volume structural applications is non-trivial. Deformation routes offer an intriguing capability in this regard due to their intrinsically scalable nature. To date, the use of deformation-based frameworks for achieving functional gradation of cellular solids has been limited to friction stir processing (FSP) [13, 14], which uses intense heat due to a friction slider to fabricate porous samples from specially mixed initial powder forms. This has been successful in creating graded cellular materials, however a limitation of the FSP method

is the inherent discrete nature of the resulting gradation (e.g., binary-type gradation) in the porous material.

In contrast, controlled deformation-based routes for achieving density gradients from bulk cellular solids have not been explicitly explored. Functional gradation by surface plastic deformation methods has received significant attention in the domain of fully-dense metals, where the near surface straining that occurs causes refinement of the surface microstructure by generation of dislocations and other defects that contribute to continuous recrystallization of microstructure [15, 16]. This functional gradation by surface severe plastic deformation routes has been shown to dramatically improve the mechanical properties of wrought material due to the attendant grain refinement. Controllability of the gradation is generally achieved by specialized tool design and control of a number of processing parameters [17].

In cellular solids, study of the role of mechanical processing in changing surface structure has been primarily limited to investigations focused on component manufacturing issues in machining and forming configurations. Several experimental studies have been made to explore the effect of machining parameters on metallic foam response [18-23]. For instance, Schoop et al. [20] utilized scanning electron microscopy (SEM)-based characterization to assess surface morphology changes with application of cryogenic cooling to machining of porous tungsten. Bram et al. [21] also utilized SEM-based observations to compare cutting and grinding approaches and their effects on subsurface damage in finishing of titanium foams. Deglurkar et al. [22]

expanded these observations and made histological measurements with optical microscopy of incremental sections of machined porous tantalum implants. While these investigations have contributed to understanding processing effects for these porous materials, prior measurements have been limited to 2D analyses instead of full volume measurements of surface integrity.

Full volume measurements of surface damage in machined foams are important for developing high fidelity understanding of machining-induced effects on foam structure and have yet to be established. New developments in X-ray-based micro-computed tomography (micro-CT) have opened advanced non-destructive options for characterization and visualization of complex 3D foam structures [24]. X-ray CT relies on measurement of local X-ray attenuation to generate high resolution 3D maps of internal structure. In terms of its metrological application, several works have sought to identify the role of controllable CT measurement variables (e.g., voltage, current, thresholding algorithm, etc.) in determining overall measurement uncertainty [25-27]. In its application for studying structure of hard foams, significant attention has focused on use of CT to establish mechanics of damage and failure of foams in generalized static loading, including in tension and compression using 3D non-destructive imaging [5, 28-32]. These studies have elucidated various underlying plastic failure phenomena for foams, including localized plastic accommodation in deformation bands [5, 30, 31] and plastic hinging mechanisms in individual foam struts by taking a series of CT images in various stages of deformation of one sample and by constructing 3D displacement maps from pairs of images [28, 31, 32].

Thermomechanical loading in surface generation by machining of porous foams is substantially more complex than that in uniaxial loading due to the intrinsic macro-scale heterogeneity present during surficial deformation. This heterogeneity gives rise to localized damage (e.g., smearing, fracture) in the immediate surface as well as a range of diffuse and localized structure damage throughout the subsurface (e.g., banding, cell damage, dilation) [33, 34]. More recently, Qiao et al. [35] has made detailed tomographic measurements of the solid network in the machining of cellular material and shown that a graded structure exists at the surface in these materials in terms of the relative pore size.

1.2. Problem Statement

The present study aims to establish the capability of surface straining by machining-based processing to control surface structure and affect mechanical performance of a structural foam. The morphological damage to the pore-strut network of the foam and post-mortem surface integrity characteristics, including effective pore size, surface area, deformation-affected zone depth, strut specific surface area, and fractured strut orientation distribution, were characterized as a function of machining parameters at full-volume using micro-computed tomography. From these observations, the subsurface damage was characterized to determine presence of spatially-graded features. To understand the effect of machining processes on the mechanical performance, the deformation behavior during the compressive loading experiments

were observed nondestructively by X-ray micro-computed tomography. To quantify the effect of the structural gradation on mechanical response and understand the underlying mechanisms, incremental displacement and strain fields were measured using digital volume correlation.

CHAPTER 2. BACKGROUND

2.1. Computed Tomography

A micro-computed tomography platform (Zeiss Metrotom 800) was utilized for full-volume structural characterization. During the tomographic scans, the workpiece was rotated incrementally over a total angular range as image projections were acquired. The X-ray tube was used under controllable power settings and the X-ray beam directed through the sample and onto a planar detector. By collecting a large number of projections from different orientations of the sample in front of the detector, a three-dimensional grayscale field was generated by use of an image reconstruction algorithm.

In terms of dimensional measurement, possible errors in the CT-based measurements can be quantified as a function of controllable CT measurement variables and analysis parameters. The resulting measurement capability analysis aids a more complete understanding of CT-based inspection methods for metrological applications, including for other complex solids, such as those produced by additive manufacturing. For this study, dimensions of gauge blocks (Mitutoyo Corporation) and gauge pins were investigated under various X-ray voltage, current, integration time and image averaging conditions to determine effect on measurement uncertainty of a number of different measures (e.g., length, flatness, parallelism) [36, 37]. The measurement algorithms used in the present study include highly controllable edge detection, and a least squares scheme for fitting of measurement planes and cylinder geometry. These measurement

algorithms are described in the ensuing.

Edge Detection Surface determination for three-dimensional edge detection is a critical factor affecting measurement uncertainty from tomographic data sets. For conventional CT analysis packages, a 50% iso-surface global threshold is typically applied, which defines the average intensity between background and material peaks in histogram so to threshold and locate a material boundary. In reality, this exact threshold value is highly dependent on material, specimen geometry and size; it has been shown that a 50% iso-surface threshold generally yields an overestimation of specimen size whereby the ideal threshold is higher intensity [38]. For the present study, a Canny edge detection algorithm was used for measurement of both the gauge pins and gauge blocks [39]. This gradient-based edge detection method includes the following procedure: (1) application of a Gaussian filter to attenuate 3D image noise with standard deviation of 1; (2) calculation of the gradient magnitude and direction for each voxel on the smoothed image; (3) comparison of the magnitude of each voxel to that of local neighbors along the direction obtained (this non-maximum suppression (NMS) guarantees that the edge is located in a single voxel level); and (4) searching for two gradient thresholds so to achieve pure and complete edges. Strong edges are located on edge candidates having gradient greater than the high threshold (e.g., step 3), whereas candidate lower than the small threshold are eliminated and those at intermediate gradients are treated as weak edges if connected with edges already stored. This procedure is generally referred to as dual-threshold hysteresis. Further, sub-voxel resolution for edge detection is enabled by quadratic polynomial fitting of the local field

of edge candidates [40]. Figure 2.1 provides an image that shows the identification of an edge on a test image for tomographic imaging of a gauge block, with the edge identified using a red line in the figure.

Cylinder fitting Surfaces for gauge blocks can be easily fitted based on classical linear least-squares algorithms. In comparison, nonlinear least squares methods should be applied for cylinder fitting in the case of gauge pins. First, the cylinder is characterized by approximating its axis and radius. The axis can is defined by a point (x, y, z), and the direction vector (a, b, c), with radius r. Second, the distance between the fitted cylinder surface and an arbitrary measured point cloud was calculated by evaluating the objective function:

$$\frac{\sqrt{(c(y_i - y) - b(z_i - z))^2 + (a(z_i - z) - c(x_i - x))^2 + (b(x_i - x) - a(y_i - y))^2}}{a^2 + b^2 + c^2} - r$$

where (x_i, y_i, z_i) is the i[th] point of the measured data cloud. The goal of this problem is to find a parameter combination of (x, y, z, a, b, c, r) that yields the global minimization of the sum of objective function squares [41]. To reduce the computational effort, the MATLAB built-in function *lsqnonlin* was applied, with initial guess based on single image slices. An example of this approach to determine cylindrical surfaces on the gauge pins is shown in Fig. 2.2.

2.2. Watershed Segmentation

A MATLAB-based 3D watershed algorithm was used to isolate and quantitatively characterize pore morphology. The analysis code assigns each pore in the low-density solid a unique label based on a three-dimensional distance map in which each voxel center has a value of the distance to the nearest solid-phase voxel and each pore centroid is located at a relative peak in the distance map [42, 43]. One typical analysis result is shown in Figure 2.3, where Figure 2.3(a) provides the volumetric rendering of a unit cell and Figure 2.3(b) shows the corresponding segmentation results.

2.3. Digital Volume Correlation

Digital volume correlation (DVC) was used to quantitatively measure the deformation field. DVC is a correlation-based 3D image analysis method used to track features of tomographic images. This image correlation technique allows for full three-dimensional (3D) strain measurement of a deforming solid. The flow chart in Figure 2.4 illustrates the basic DVC procedure employed in this study. 3D images with dimensions M x N x P are extracted from the X-ray CT at time points t and t+dt. The displacement field between these image frames is measured on a virtual grid set, this providing a discrete array of analysis sites in the measured volume. Therefore, a set of artificial grids with spacing m x n x p is imposed on the reference (original) volume and deformed volume. At each grid, a sub-volume, or what can be considered the equivalent of an interrogation window, with size of M' x N' x P' is defined. Typically,

the size of the sub-volume M' x N' x P' is the grid size m x n x p multiplied by a factor of 2 to 4. A margin region is also delineated in case that any sub-volume in the reference frame is correlated with counterpart outside the deformed frame. Several regions with zero or constant displacement are also masked to save computation time. A schematic depicting 3D image information, grid and sub-volume settings mentioned above is provided in Figure 2.5. In this particular case, adjacent grids represented by blue points are equally spaced by 50 voxels and the representative rectangular sub-volume is indicated by dash lines with dimensions of 101 x 101 x 101 voxels (i.e., double spacing of the grid size) and centered on the grid at the left bottom corner.

The next step in the algorithm is to quantify the motion of the material in each sub-volume, indicative of the average spatial offset of material contained within it. This offset is measured between subsequent image frames using the statistical technique of cross-correlation, this defining a deformation in the sub-volume. The cross correlation between the sub-volume in the reference image (f) and the sub volume in the deformed image (g) is defined as $f * g = \sum_{x=1}^{m} \sum_{y=1}^{n} \sum_{z=1}^{p} f(x,y,z) g(x+i, y+j, z+k)$, where (i, j, k) represents the peak value of the cross correlation and the displacement vector. This cross correlation quantifies the degree of similarity of gray level distributions, and can be computed in either the spatial domain directly or the frequency domain, the latter preferred due to its computational efficiency. By the theorem [44], $f * g = IFFT\ (FFT(f) \times \overline{FFT(g)})$, where FFT is the Fast Fourier Transform, $IFFT$ the inverse Fast Fourier Transform, and top bar indicates complex conjugate. As shown in Figure 2.5, in the case that the reference sub-volume f and the corresponding

target sub-volume g are identical, the resultant cross correlation field has a maximum value at the sub-volume center, this shown as a single high valued point and corresponding to a measured displacement of zero. This correlation procedure is repeated for each grid in the imaged region, to obtain a complete displacement field for each image-pair. For removing possible outliers, a zero mean normalized cross-correlation (ZNCC) coefficient is defined in the range of -1 to 1 as below, and calculated to check quality of match using the expression [45-48]

$$C_{ZNCC}(u,v,w) = \frac{\sum_{i=1}^{s}[f(x_i,y_i,z_i) - f_m][g(x_i+u,y_i+v,z_i+w) - g_m]}{\sqrt{\sum_{i=1}^{s}[f(x_i,y_i,z_i) - f_m]^2}\sqrt{\sum_{i=1}^{s}[g(x_i+u,y_i+v,z_i+w) - g_m]^2}}$$

where $f(x_i,y_i,z_i)$ and $g(x_i+u,y_i+v,z_i+w)$ are the grayscale values of the ith voxel in the reference and target sub-volume, f_m and g_m represent mean intensity values of the corresponding sub-volumes, and u, v, w are the estimated displacement values in the x, y, z directions respectively. The outliers are replaced by interpolated values from the surrounding valid ones through an interpolation exercise of cubic splines. In this analysis, a ZNCC coefficient of 0.6 was utilized as a threshold to determine if a value is an outlier.

As discussed above, an initial full field estimation of motion can be completed efficiently through FFT-based cross correlation. However, the estimated values are generally not sufficiently accurate in practice [49] and an optimization approach is needed. In this case, a linear intensity change model [46] was used to take into account probable intensity pattern change of scanned samples even under the same power and

exposure settings. This model can be described as the equation of $g(x_i', y_i', z_i') = af(x_i, y_i, z_i) + b$ for a sub-volume, where a and b are two unknown parameters accounting for the scale factor and the offset of the intensity change. Following that, an iterative least squares algorithm [46] was implemented to achieve sub-voxel accuracy of the deformation field. In addition, the linear displacement mapping function was necessary to involve possible strain, rotation as well as translation and is defined as,

$$\begin{bmatrix} x_i' \\ y_i' \\ z_i' \end{bmatrix} = \begin{bmatrix} x_0 \\ y_0 \\ z_0 \end{bmatrix} + \begin{bmatrix} \Delta x_i \\ \Delta y_i \\ \Delta z_i \end{bmatrix} + \begin{bmatrix} u \\ v \\ w \end{bmatrix} + \begin{bmatrix} u_x & u_y & u_z \\ v_x & v_y & v_z \\ w_x & w_y & w_z \end{bmatrix} \begin{bmatrix} \Delta x_i \\ \Delta y_i \\ \Delta z_i \end{bmatrix}$$

where Δx_i, Δy_i, Δz_i are the distance components from the grid (x_0, y_0, z_0) to point (x_i, y_i, z_i), u, v, w are the displacement components for the grid in the x, y, z directions, and u_x, u_y, u_z, v_x, v_y, v_z, w_x, w_y, w_z are the displacement derivatives of the sub-volume [29, 46, 50].

To optimize results from the cross correlation, a model function was first defined as $F_i(\vec{p}) = g(x_i', y_i', z_i') - af(x_i, y_i, z_i) - b$, with the deformation parameter $\vec{p} = \left(u, u_x, u_y, u_z, v, v_x, v_y, v_z, w, w_x, w_y, w_z, a, b\right)^T$, where $\vec{p}^0 = (u, 0, 0, 0, v, 0, 0, 0, w, 0, 0, 0, 1, 0)^T$ obtained by FFT can be used as the starting point of iteration. In a classical non-linear least squares scheme, $S = \sum_{i=1}^{n} F_i^2$ is minimized to best fit the parameters, in other words, the gradient with respect to $\vec{p}$ is zero, i.e., $\frac{\partial S}{\partial p_j} = 2\sum_{i=1}^{n} F_i \frac{\partial F_i}{\partial p_j} = 0$, $(j = 1,2, \ldots, 14)$. Successive approximations are necessary i.e., $p_j \approx p_j^{k+1} = p_j^k + \Delta p_j$, where k is the iteration count, Δp_j is the correction term. Then, first-order Taylor series expansion is operated about p_j^k: $F_i \approx F_i^{k+1} =$

$F_i^k + \sum_j^{14} J_{ij}^k \Delta p_j$, where the Jacobian $J_{ij}^k = \frac{\partial F_i^k}{\partial p_j}$. Final substitution into gradient equation: $\sum_{i=1}^{n}(F_i^k + \sum_q^{14} J_{iq}^k \Delta p_q) J_{ij}^k = 0$

$$\sum_{i=1}^{n} F_i^k J_{ij}^k + \sum_{i=1}^{n}\sum_{q}^{14} J_{ij}^k J_{iq}^k \Delta p_q = 0$$

$$\vec{J}^T \vec{F}(\vec{p}^k) + \vec{J}^T \vec{J} \Delta \vec{p} = \vec{0}$$

$$\Delta \vec{p} = -\left(\vec{J}^T \vec{J}\right)^{-1} \vec{J}^T \vec{F}(\vec{p}^k)$$

To illustrate the iterative optimization approach, Figure 2.6 provides a graphical depiction of the schematic. For convenience, the reference volume and deformed volume are drawn in a single 3D image frame. In Figure 2.6(a), a representative reference sub-volume is shown as a cube by dashed lines, and the corresponding target sub-volume as a parallelepiped by solid lines, this shape indicative of translation and strain experienced between frames. In Figure 2.6(b), the reference sub-volume has experienced a simple translation $\vec{p}^0$, and further search for optimal deformation parameters is necessary to bring the sub-volume close to the target one. After several iterations, the optimization process for the current grid is completed and the effect is shown in Figure 2.6(c). Finally, cubic spline interpolation is employed to extract the sub-voxel gray scale intensity information.

To evaluate the accuracy and standard deviation of the DVC code created, a series of simulation tests are typically used [46]. For this purpose, a baseline 3D image was generated with a random distribution of spherical particles, as shown in Figure 2.7. The

frame bounded by the black box has a dimension of 400 x 400 x 400 voxels, and the number of particles is $s = 10000$, with each particle having a constant radius R of 6 voxels. The 3D image pair was generated according to the following equations:

$$I(x,y,z) = \sum_{k=1}^{s} I_k exp\left[-\frac{(x-x_k)^2 + (y-y_k)^2 + (z-z_k)^2}{R^2}\right]$$

$$\hat{I}(x,y,z) = \sum_{k=1}^{s} I_k exp\left[-\frac{(x-\hat{x}_k)^2 + (y-\hat{y}_k)^2 + (z-\hat{z}_k)^2}{R^2}\right]$$

where $I(x,y,z)$ and $\hat{I}(x,y,z)$ are intensity fields before and after deformation, I_k is the peak intensity value of the k[th] particle. The deformation field was defined as $\begin{bmatrix}\hat{x}_k \\ \hat{y}_k \\ \hat{z}_k\end{bmatrix} = \begin{bmatrix}x_k \\ y_k \\ z_k\end{bmatrix} + \begin{bmatrix}u \\ v \\ w\end{bmatrix} + \begin{bmatrix}u_x & u_y & u_z \\ v_x & v_y & v_z \\ w_x & w_y & w_z\end{bmatrix}\begin{bmatrix}x_k \\ y_k \\ z_k\end{bmatrix}$. By setting the $\begin{bmatrix}u \\ v \\ w\end{bmatrix}$ and $\begin{bmatrix}u_x & u_y & u_z \\ v_x & v_y & v_z \\ w_x & w_y & w_z\end{bmatrix}$ matrices, the image pair with certain intensity and deformation field was created.

In this study, simulated translation and uniform compression displacement fields were evaluated with various grid sizes GS = {13, 19, 25} voxels and sub-volume sizes SS = {51, 75, 99} voxels. The schematic provided in Figure 2.8 illustrates the artificial deformation process in both cases. In particular, Figure 2.8(a) indicates the reference state of the shaded object, filled with spherical particles, and Figure 2.8(b) and 2.8(c) show the translated state and compressed state on the top of the object, respectively. The predefined displacement values are {0, 0.4, 0.8, 1.6, 3.2, 4, 8, 12, 16, 20, 24} voxels, and strain values are {2%, 4%, 6%}. The test results are plotted in Figure 2.9. Figure 2.9(a) suggests that the mean bias of integer voxel displacement is in the order of 1.0 x

10^{-6} voxels, and insensitive to the different grid and sub-volume sizes. In contrast, the bias from sub-voxel displacement can reach up to 1.0 x 10^{-5} voxels, ten times greater than in the integer displacement cases. Figure 2.9(b) implies that the standard deviation in the case of sub-voxel displacements can vary from 1.4 x 10^{-5} to 4.0 x 10^{-6} voxels, depending on the window size, and generally large sub-volume tends to yield high precision. Figure 2.9(c) and (d) indicate the mean bias and standard deviation varying with the input nominal compressive strain. Basically, small deformation and large sub-volume size gave rise to high accuracy and precision, which are insensitive to the grid spacing. In addition, the standard deviation changed linearly with the input strain, and a large sub-volume yielded a low slope, this indicating that the precision was relatively stable to parameters.

The artificial deformation tests on ideal 3D images help to quantify the uncertainties from DVC itself. However, in experiment, images are collected from real CT machines and this may provide an additional source of uncertainty. Thus, it was necessary to evaluate the uncertainty by applying the artificial deformation to the real reconstructed images with a known solution [51]. Two consecutive scans on a foam sample were conducted under the same settings as in the experiment discussed in the ensuing, and the artificial deformation was applied to one of the two baseline images by calculating the analytical displacement field at each voxel and evaluating it based on spline interpolation in MATLAB. The DVC was performed on the image pair to generate quantitative results. The representative image pairs for artificial translation and compression are rendered in Figure 2.10. The test results are shown in Figure 2.11.

Figure 2.11(a) indicates that the mean bias of displacement was relative constant in the order of 3.3×10^{-2} voxels and Figure 2.11(b) shows that the standard deviation varied from 2.0×10^{-2} to 6.0×10^{-2} voxels when sub-volume side length changed from 99 to 51 voxels. Both mean bias and standard deviation are higher than in the case of ideal images. Figure 2.11(c) and (d) indicate that the mean bias and standard deviation are constant with the input nominal compressive strain and in the same order as shown in Figure 2.9(c) and (d). As expected, a larger sub-volume yielded high accuracy and precision.

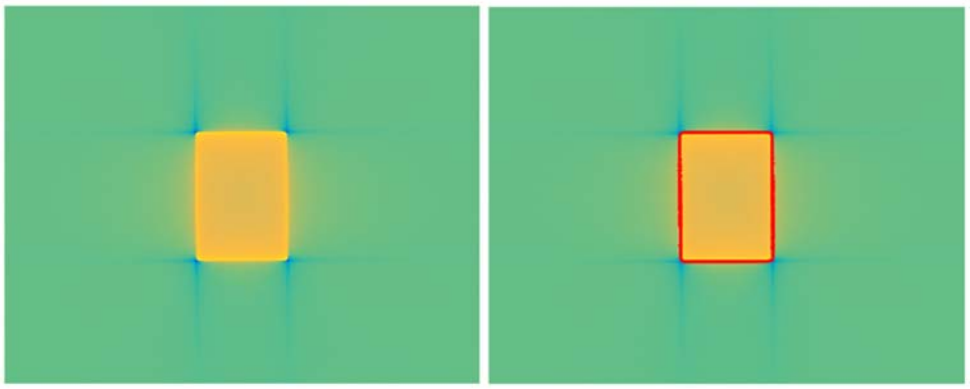

(a) (c)

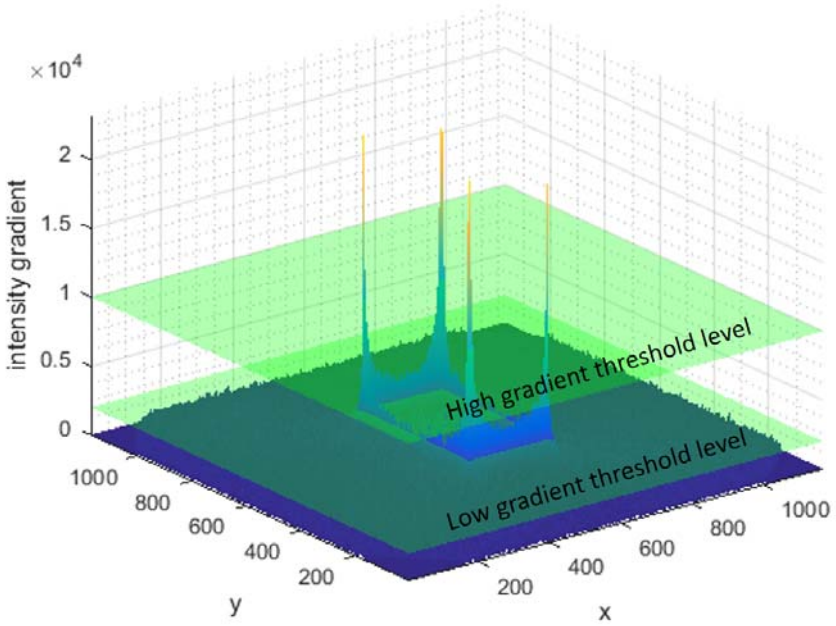

(b)

Figure 2.1. (a) Gaussian filtered image for gauge block of 5 mm; (b) gradient distribution with empirical dual threshold selections; (c) edge detection result.

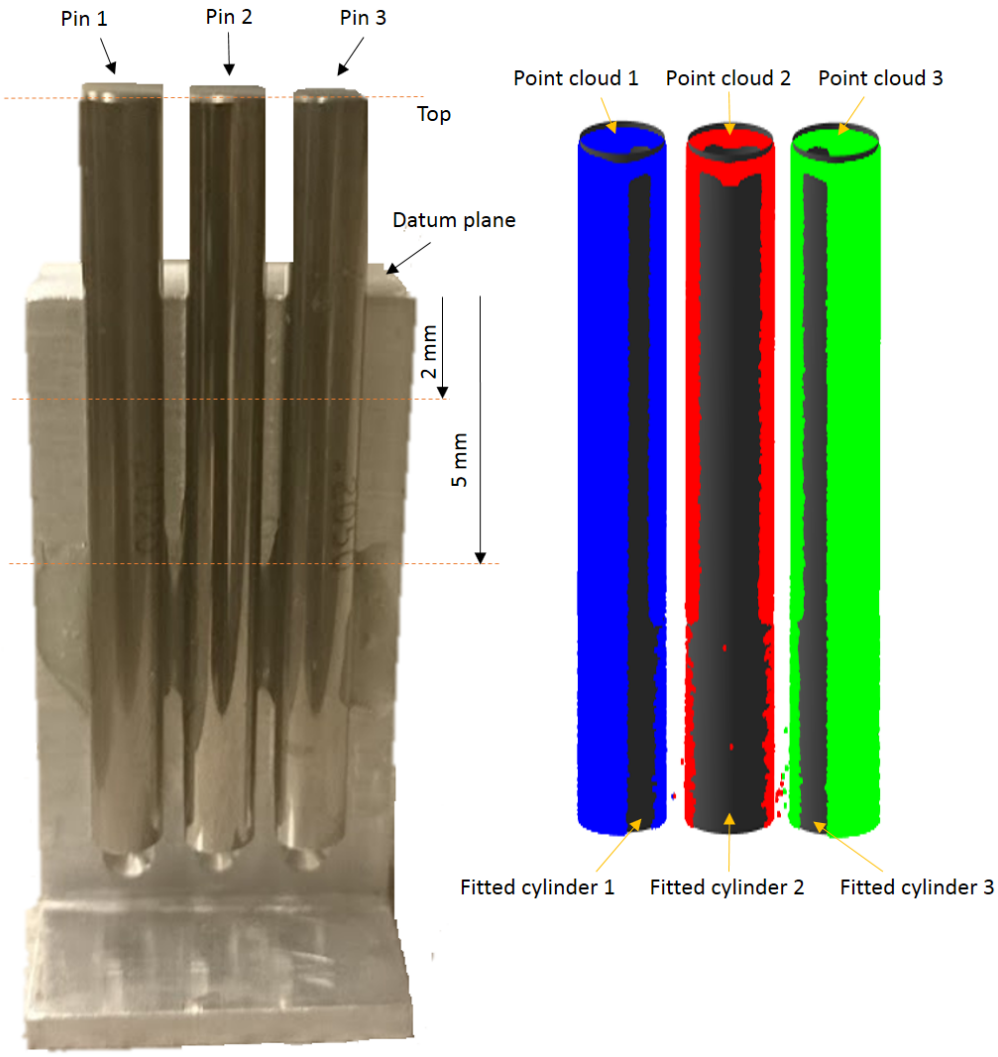

Figure 2.2. Gauge pins specimen with datum plane and measurement locations as indicated, and point cloud obtained by Canny algorithm and fitted cylinder.

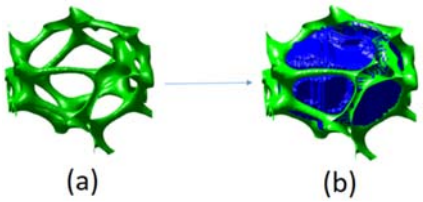

Figure 2.3. (a) the voxel model of a representative unit cell in cellular solids; (b) watershed segmentation of the pore.

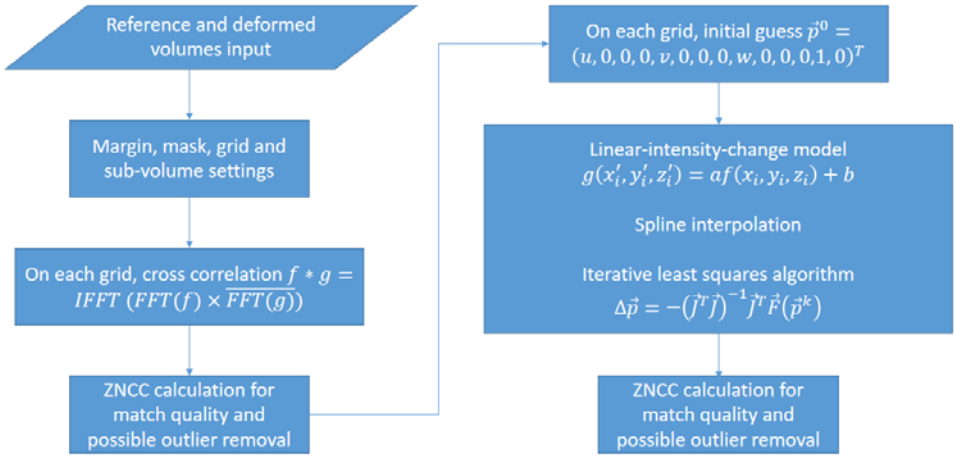

Figure 2.4. Digital volume correlation (DVC) procedure implemented in this study.

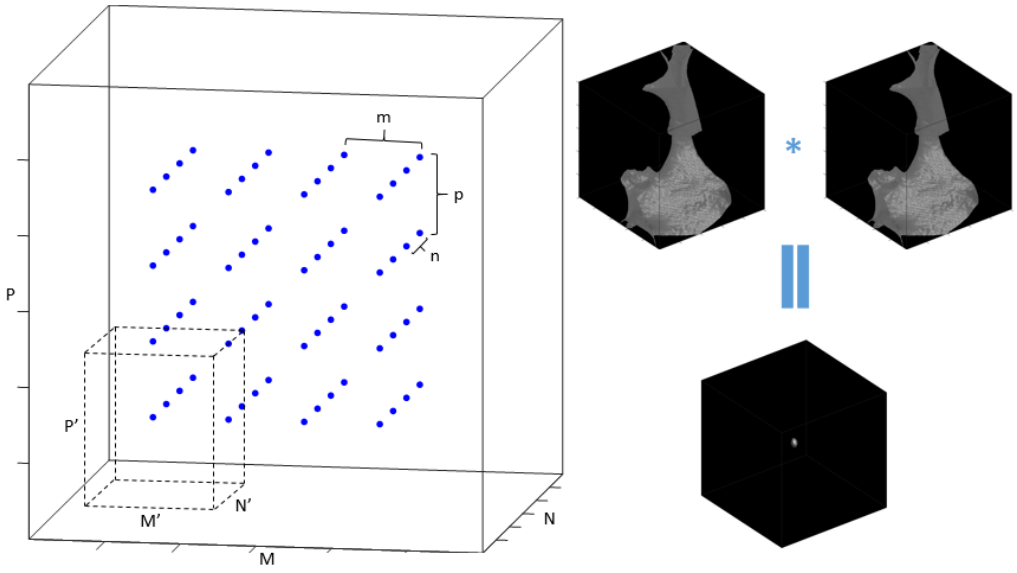

Figure 2.5. Grid and sub-volume setting, and a schematic of a typical cross correlation process.

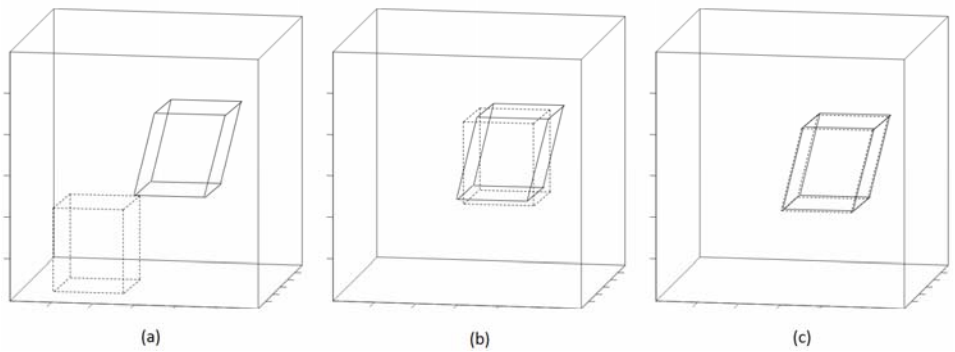

Figure 2.6. A schematic of the iterative scheme to search for the optimal deformation parameter.

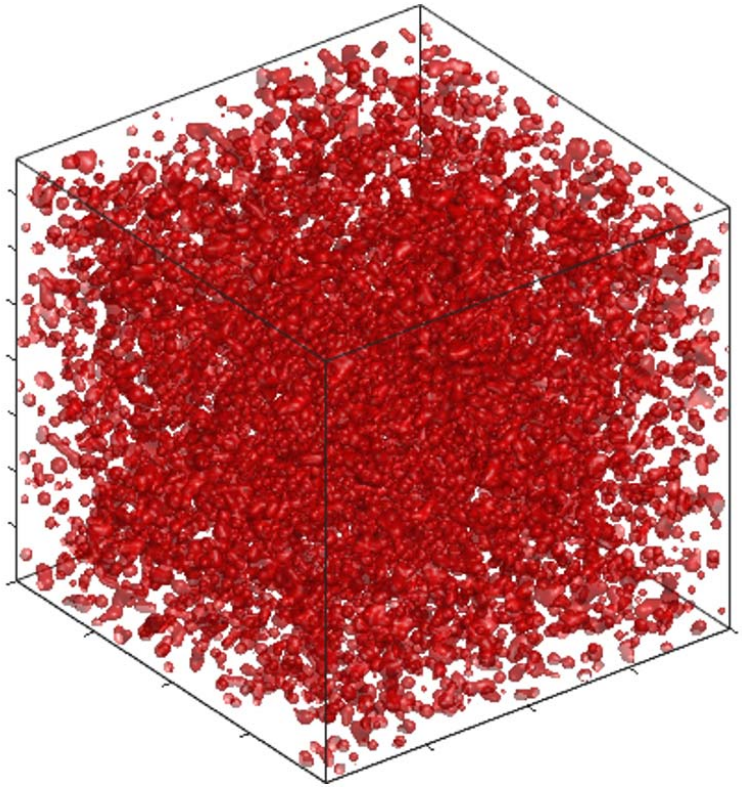

Figure 2.7. The particle field used in the simulation process.

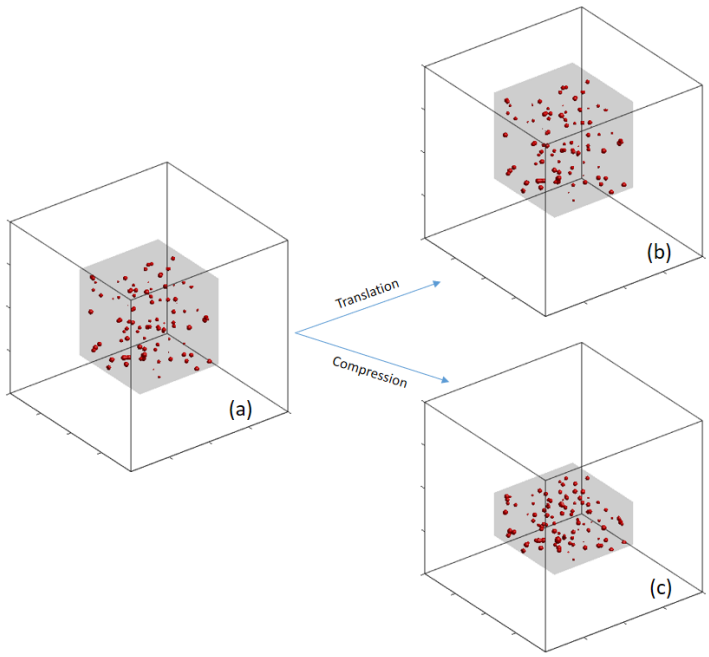

Figure 2.8. A schematic of artificial deformation in the object filled with particles.

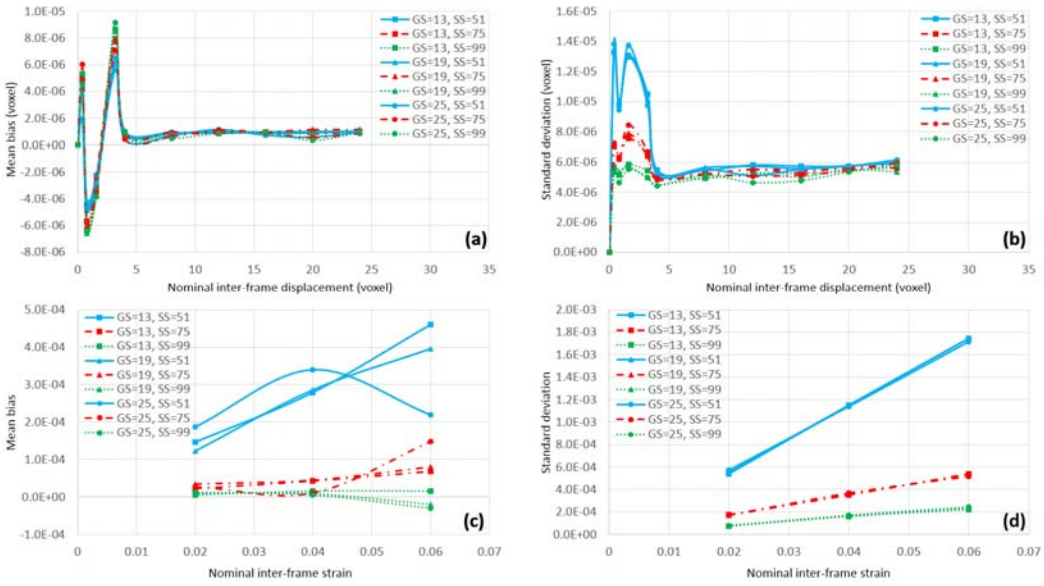

Figure 2.9. DVC calibration result: (a) mean bias of various displacements, (b) standard deviation of various displacements, (c) mean bias of three strain levels, and (d) standard deviation of three strain levels under different grid and sub-volume settings on artificial 3D images.

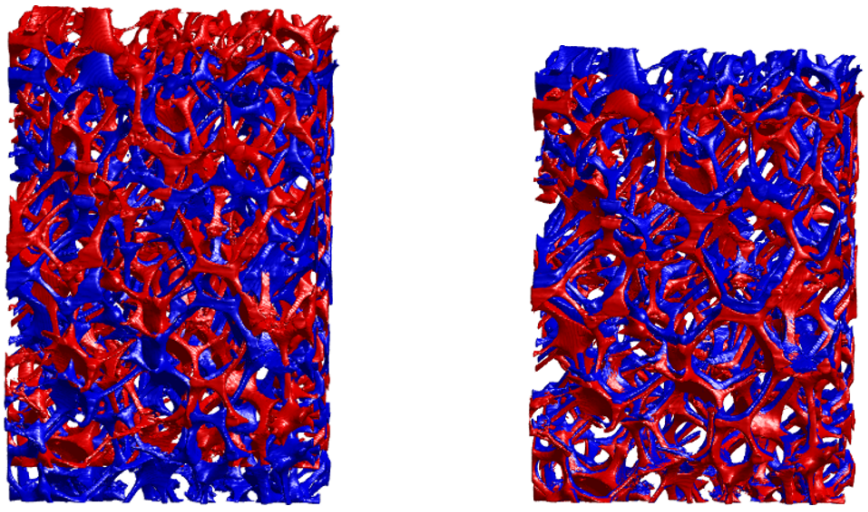

Figure 2.10. (a) baseline image 1 (blue) and baseline image 2 (red) artificially translated by 24 voxels; (b) baseline image 1 (blue) and baseline image 2 (red) artificially compressed by 6%.

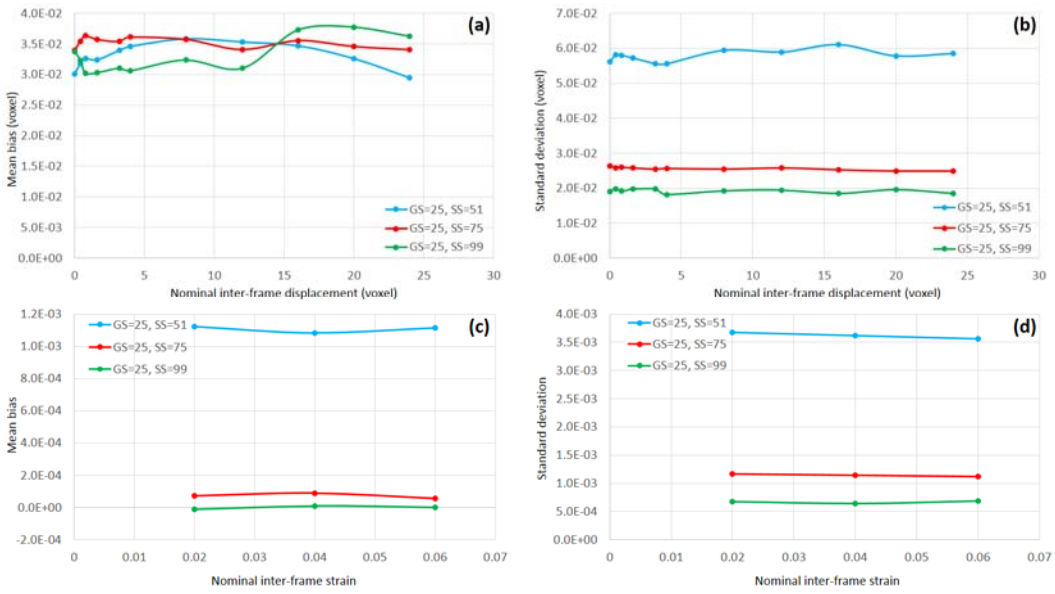

Figure 2.11. DVC calibration result: (a) mean bias of various displacements, (b) standard deviation of various displacements, (c) mean bias of three strain levels, and (d) standard deviation of three strain levels under different grid and sub-volume settings on real reconstructed 3D images.

CHAPTER 3. EXPERIMENTAL

3.1. Machining of Metal Foams

First, a milling operation on open-cell Al foams was carried out using a face mill having a diameter of 50 mm with two square Fansteel SEC-422/2A5 uncoated carbide inserts (rake angle 6°). The work samples used in this study were open-cell Duocel 6101-T6 aluminum alloy foams in the form of 89 mm x 38 mm x 12 mm rectangular blocks, with a relative density of 7% ~ 9% and an average pore diameter of 2.2 mm nominally. The machining plaftorm, a Proto Trak K3 SMX Knee Mill, was used to machine the specimen surface in a single machining pass at cutting speeds of v_c = {2.6, 3.7, 5.2 m/s}, feed rates of v_f = {0.051, 0.102, 0.204 mm/min}, and axial depths of cut a_p = {1.0, 1.5, 2.0 mm}. The experimental matrix and schematic diagram are shown in Table 3.1 and Figure 3.1, where ND, TD and FD represent normal, transverse and feed directions respectively.

Using a micro-computed tomography platform (Zeiss Metrotom 800) with an effective spatial resolution of 57.32 μm/voxel, structural characterization of the initial and post-machined foam samples was performed. The tungsten X-ray tube of the tomographic platform was used under scanning conditions of 80 kV and 100 μA, corresponding to an 8 μm focal spot size. During the tomographic scans, the original and deformed foam samples were rotated in incremental steps of 1/4 degrees over a total angular range of 360 degrees as three-dimensional images are acquired. The X-ray beam directed

through a sample mounted on a rotational stage was recorded on a planar detector, including a 1536 pixel x 1900 pixel chip with a unit pixel of 127 μm x 127 μm, this used in a 1 x 1 or 2 x 2 binning mode.

By collecting a large number of projections from different orientations of the sample in front of the detector, the Feldkamp-type cone-beam filtered back projection reconstruction provided three-dimensional map of the effective attenuation coefficients within the sample, in terms of gray levels corresponding to the average density inside each voxel. This map formed 3D image and individual 2D image slices of the three-dimensional solid with each slice in .tiff format corresponding to unit voxel thickness. Figure 3.2 (a) shows typical reconstructed images with high contrast between the aluminum (2.7 g/cm^3) and the air (0.00119 g/cm^3), such that an ISO50 threshold was given by the average of the modes for the air phase and solid phase shown in Figure 3.2(b). A binarization process based on the threshold facilitated the distinction between the aluminum and pore space to create 3D volumetric renderings of the foam structures, watershed segmentation and medial axis extraction [52].

3.2. Compression Tests

For uniaxial compression tests, rectangular specimens were extracted from an unmachined sample and a machined sample using a wire-cut electrical discharge machining (EDM) system, this minimizing mechanical distortion along sample edges. The specimens had a square cross section, approximately 5 cells wide (10 mm x 10

mm), and a height of 16 mm (i.e., approximately 7 cells). To investigate the effect of machining on the mechanical behavior of gradient foam, the machined surface was oriented perpendicular to the compression loading direction so that heterogeneous response in the unmachined and machined samples under compression could be visualized and analyzed at every step from the nominal strain of 0% to 60%, as shown in Figure 3.3. In the leftmost portion of the figure, photos of an unmachined sample and a machined sample are provided. The rightmost portion of the figure shows voxel models of the two samples and the single cell cross section to study. The specimens were compressed between rigid parallel plates in a specially designed electromechanical loading stage under displacement control at a constant rate of 0.4 mm/s, with load – displacement response recorded. The uniaxial displacement imposed to the sample was provided by a computer controlled stepping motor.

In order to characterize the cell and strut morphology, and subsequently observe the in-situ internal microstructure evolution after each compressive step, the loading stage was mounted on the rotational stage between the X-ray source and the detector in the micro-computed tomography platform. At each step of compression, the specimen was rotated in incremental steps of 1/4 degrees over a total angular range of 360 degrees as three-dimensional images were acquired. The tungsten X-ray tube of the tomographic platform was used under scanning conditions of 120 kV and 65 μA, this corresponding to an 8 μm focal spot size. The exposure time was set to 0.8 s and the X-ray beam passing through the specimen was recorded on the planar charge-coupled device (CCD) detector. The voxel size was 50.94 μm and the total duration of a single scan was

approximately 70 minutes. To measure the inter-frame local deformation fields, the digital volume correlation (DVC) was implemented in MATLAB, with the grid spacing equal to 21 x 21 x 21 voxels and sub-volume size of 81 x 81 x 81 voxels.

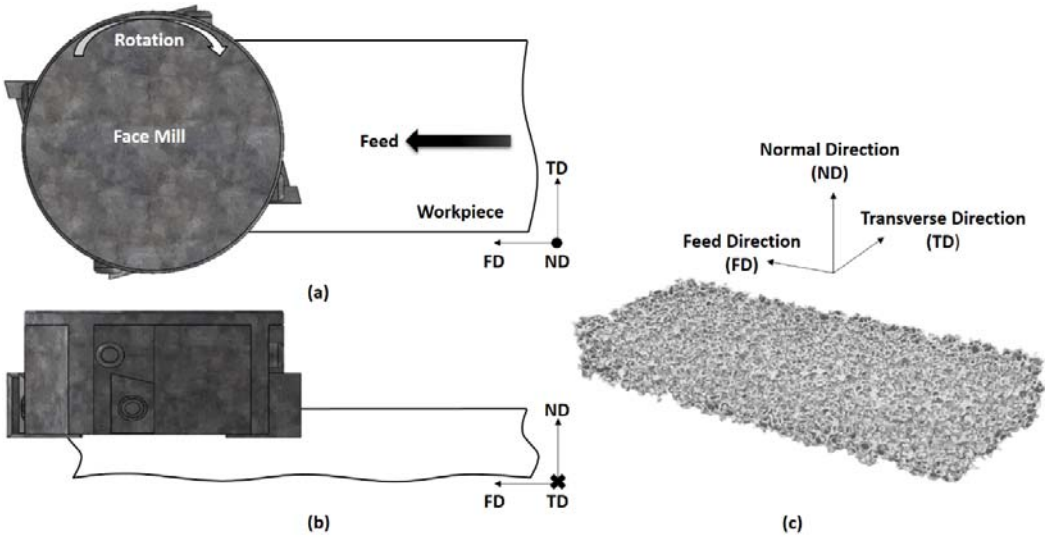

Figure 3.1. Schematic diagram of the face milling process from (a) top view and (b) side view on (c) an open-cell aluminum foam sample.

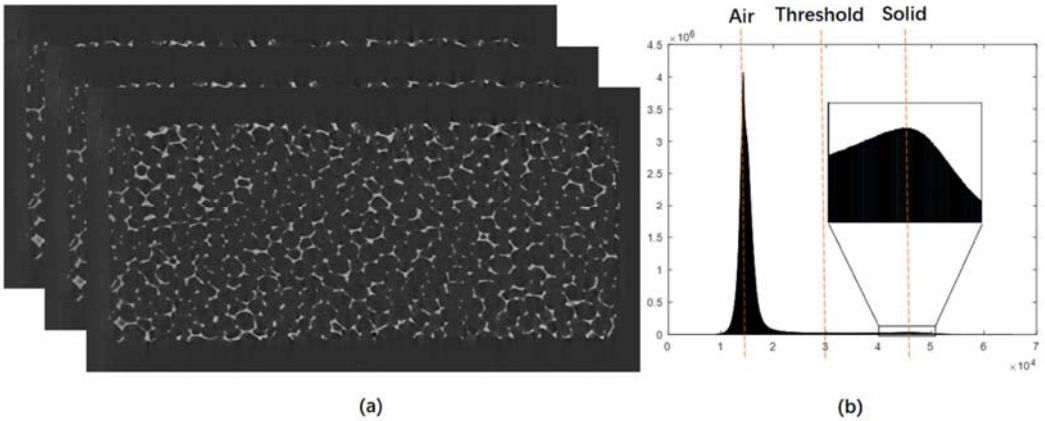

Figure 3.2. (a) Representative reconstructed image slices; (b) gray scale intensity histogram of 3D reconstructed volume, with air mode, solid mode and threshold value marked by dash lines.

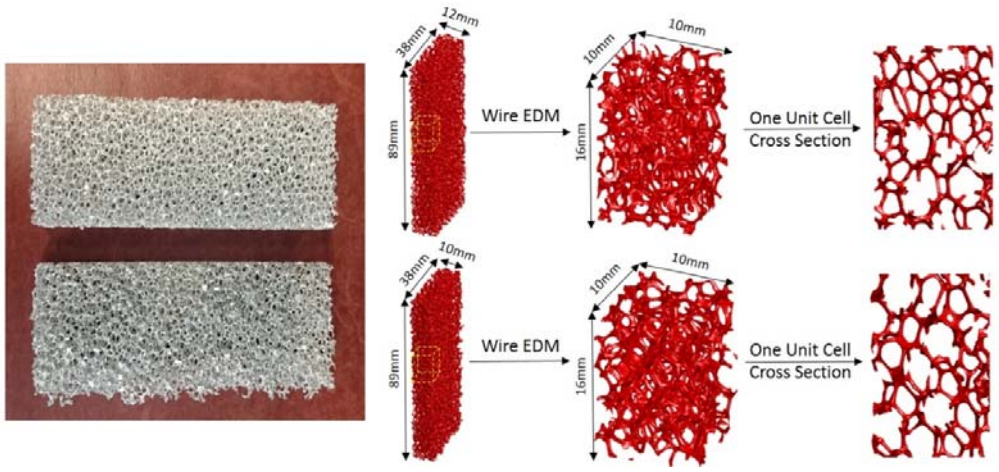

Figure 3.3. Photographs and voxel models of original and machined samples, with small specimens cut by wire EDM for compression tests.

Table 3.1. Experimental matrix during face milling processes.

Experiment	Cutting speed (v_c) (m/s)	Feed per tooth (v_f) (mm/min)	Depth of cut (a_p) (mm)
E01	2.6	0.051	1.0
E02	2.6	0.051	1.5
E03	2.6	0.051	2.0
E04	2.6	0.102	1.0
E05	2.6	0.102	1.5
E06	2.6	0.102	2.0
E07	2.6	0.204	1.0
E08	2.6	0.204	1.5
E09	2.6	0.204	2.0
E10	3.7	0.051	1.0
E11	3.7	0.051	1.5
E12	3.7	0.051	2.0
E13	5.2	0.051	1.0
E14	5.2	0.051	1.5
E15	5.2	0.051	2.0

CHAPTER 4. RESULTS AND DISCUSSION

4.1. Subsurface Integrity in Face Milling of Metal Foams

The effects of face milling parameters on the surface structure of the foam samples was observed in terms of structural changes to both solid strut configurations and the resulting pore morphology. Figure 4.1 is a graphical representation of voxel models for both the initial and post-machined foam samples under the condition E08 in Table 3.1 (i.e., v_c = 2.6 m/s, v_f = 0.204 mm/min, a_p = 1.5 mm), obtained at subsurface depths of 1.5 and 8.5 mm from the machined surface, as well as the resulting pore morphology and strut network, based on the MATLAB-based tomographic analysis.

The figure shows that close to the machined surface, strut bending and fracture occur resulting in new surface branch formations, also an initial pore was divided into sub-pores with respect to volume change associated with local strut bending and multiple local distance maxima form in the distance map originally having a single maximum. Far from the machined surface, the change was negligible visually. To assess morphological changes to the strut network, Figure 4.1(c) shows the medial axis extraction results for the voxel model of Figure 4.1(a). Formation of new strut branches occurred with greater frequency close to the machined surface, likely caused by strut fracture within the deformation zone. In the following sections, the effects of machining parameters on effective pore size and surface strut curvature were mapped as a function of distance from the machined surface to quantify deformation-induced effects.

4.1.1. Characterization of Pore Morphology

To determine the effects of machining processes on subsurface integrity, Figure 4.2 – 4.4 detail the evolution of the effective pore size as a function of subsurface depth for different experimental conditions. Each pore was characterized by its centroid, which was located at a relative maximum in the local distance map. The equivalent pore diameter was evaluated by treatment of each pore as an ideal sphere, and the volume by summing the number of pore voxels based on the unique labels resultant from watershed segmentation and multiplying by the volume of one voxel. Similarly, pore surface area was calculated by summing the boundary voxels for each marked region.

To determine the effect of machining parameters on surface integrity in the milling of the hard foams, the size of the deformation-affected zone was determined from these figures based on the relative difference between the subsurface pore diameter curves for the initial and post-machined samples. For this purpose, a 98.5% threshold relative to the initial pore size was used to determine the deformation zone length. For example, in Figure 4.2 for condition (a) v_c = 2.6 m/s, v_f = 0.051 mm/min, a_p = 1.0 mm, the initial aluminum foam had an equivalent pore diameter of 2.2 mm. The foam structure up to a subsurface depth of 2.8672 mm was altered by the material removal process while deeper extents of the work material remained unaffected by deformation. Close to the machined surface, the equivalent pore diameter decreased to approximately 0.5 mm because of structural deformations (e.g., strut fracture and bending). These effects were

evident in the morphological evolution of the sets of pores identified in the inset images of Figure 4.2(a) as pairs A-A' and B-B'. In the deformation zone, pore A deformed substantially and decreased in size to A'. In contrast, pair B and B' in the far field exhibited no evidence of deformation or size changes. For condition (b) v_c = 2.6 m/s, v_f = 0.051 mm/min, a_p = 1.5 mm, the initial foam again had an effective pore diameter in the range of 2 mm, which deformed to approximately 0.5 mm in the vicinity of the machined surface. In contrast to the size of the deformation zone under condition (a), that under condition (b) increased to roughly 3.6123 mm. Finally, for condition (c) v_c = 2.6 m/s, v_f = 0.051 mm/min, a_p = 2.0 mm, the size of the deformation zone increased to 4.0172 mm with a similar limiting pore size of 0.5 mm.

Figure 4.2 demonstrates that the deformation zone increased as the depth of cut increased. Similarly, deformation zone size increased with increasing feed and decreasing cutting speed, as shown in Figure 4.3 and 4.4, respectively. For all conditions, as the distance from the machined surface increased, the effective pore diameters of the machined foam samples approached those of the initial undistorted foam samples and the pore surface area showed consistent pattern, this implying that the deformation could be characterized by either measurement. In Figure 4.5, the effects of machining parameters on deformation zone size are summarized. At a constant cutting speed of v_c = 2.60 m/s and feed rate of v_f = 0.05 mm/min, the deformation zone length ranged from 2.8 mm to 4.0 mm, this increasing with the axial depth of cut. The same trend relative to axial depth of cut persisted at higher feed rates, and deformation zone lengths were consistently higher with higher feed rates. Further, at a constant feed

rate of v_f = 0.05 mm/min, increasing cutting speed from v_c = 2.60 m/s to v_c = 5.20 m/s resulted in smaller deformation zone lengths for every axial depth of cut. Further, the aggregate results provided in Figure 4.5 indicate that pore structure changes in the milling process was most sensitive to feed and least to cutting speed for the range of machining parameters selected. From this data, it is clear that the lowest cutting speed caused up to four layers of structural cell units of the foam to be affected by surface milling wherein the machined sample thickness contained a total of five layers. In contrast, the lowest feed restricted the deformation zone extent to one layer, regardless of the cutting speed used.

4.1.2. Characterization of Strut Deformation

As shown in Figure 4.1, solid struts in the machined surface undergo fracture and bending during the material removal process. Figure 4.6 and 4.7 summarize two measurements of the strut deformation for a select number of experimental conditions. In the first row of each figure, the specific surface area of the foam was determined. This quantity is generally utilized to characterize permeability of cellular materials and is defined as external strut surface area per unit bulk volume [53]. It can be expected that strut fracture yields new surface formation and an increase of this specific surface area. Under all test conditions, the specific surface area increases in a zone approximately a single unit cell level in extent, this indicating that only one layer of the foam opens to fracture after the face-milling process. In the second row of Figure 4.6 and 4.7, stereographic projections are provided to summarize the final strut orientation

distributions. These pole figures were calculated using the fixed node and midpoint in each strut segment [54]. From the figures, the strut orientations in the original samples had no preferred orientations (e.g., random). In comparison, the machined surface struts were found to be highly concentrated in the sample normal direction (ND).

Subsurface deformation in the solid phase network was also measured by quantitative evaluation of orientation changes in the individual struts in terms of mean bending angle and formation of preferential orientation along specific specimen directions, based on medial axis extraction, in which medial axial voxels were classified as either end nodes or points in struts based upon their connectivity difference. Strut orientation was determined using the end nodes and bending angle by tracking each node and its local connectivity. Figure 4.8 shows the effect of feed rate on bending angle for individual foam struts versus subsurface depth. From the figure, it is clear that the maximum bending angle and largest plastic-affected zone corresponded to conditions of maximum feed rate. At a feed rate of v_f = 0.204 mm/min, the estimated bending angle at the free surface was 24 degrees, this decaying to near zero at subsurface depths exceeding d = 4 mm from the machined surface. The maximum bending angle on the machined surface decreased to 7.5 degrees and 2.5 degrees at feed rates of v_f = 0.102 mm/min and v_f = 0.051 mm/min, respectively, with a standard deviation of 1.3 degrees in each case. The extent of the deformation-affected layer did not appear to be as large as that seen for the corresponding conditions in Figure 4.3, as strut bending was not as significant at larger subsurface depths when compared to changes in average pore size.

4.1.3. Discussion

A direct mapping of the deformation in the solid strut network was also established using DVC. In DVC, the solid is discretized into volumetric grid elements (VGEs) each containing an equal number of voxels. For the initial and post-machined workpiece samples, the aggregate intensity of each VGE is modified by the relative motions and deformations occurring within the solid network. The relative displacement of each VGE is determined by a cross correlation of successive imaging frames and the overall displacement field is determined by iterating over all VGEs. From the displacement field, effective strain fields are determined by spatial differentiation.

Figure 4.9 shows subsurface strain distributions for workpieces machined across a range of machining conditions. From the figure, it is clear that a region of high strain persisted near the top of the workpiece in the vicinity of the cutting zone. This maximum effective strain of approximately 0.2 decayed with increasing depth into the work material subsurface until no visible plastic deformation was measured by the DVC algorithm. To assess the size of the plastic zone as a function of machining parameters, Figure 4.9(a)-(b) and Fig. 4.9(c)-(d) show the effect of feed rate for two different axial depths of cut. As cutting speed was observed in the above analyses to have a less pronounced effect on the subsurface damage, this parameter was held constant. From the subsurface strain fields, an effective strain threshold of 0.08 was used to map the deformation zone length. For Fig. 4.9(a)-(d), this resulted in deformation zone lengths of L = {2.01, 5.73, 1.43, 3.44 mm}, respectively. These measurements and the associated trends are comparable to those obtained by the watershed-based

measurement above, which yielded deformation zone lengths of L = {4.35, 6.79, 3.34, 5.01 mm}. These results are useful for higher fidelity measurement of surface integrity in foam machining.

4.2. Surface Integrity Effects on Mechanical Performance

To summarize the effect of face-milling process parameters on the subsurface porosity, the profile of equivalent pore diameter along the distance from machined surface is summarized in Figure 4.10, which was calculated using the watershed segmentation. The diameter was normalized by the average pore size (2.2 mm) of the original sample to give a relative measure of the pore size change. From the figure, it is clear that local smearing on the machined surface caused the formation of smaller pore size than in the original sample. In comparison, pores far from the machined surface were found to be nearly equal in size to that of the original foam structure, this suggesting little effect of machining on the part far from the machined surface. As with the prior experimental data, the three solid curves in Figure 4.10(a) indicate that the deformation affected zone increased with high feed rates. Similarly, in Figure 4.10(c), higher depth of cut yielded a larger region over which the pore size is affected by the machining process. The effect of cutting speeds was substantially less pronounced, as is indicated in Figure 4.10(b). In each of these plots, the curve representing the most aggressive machining condition was plotted using a dashed line for comparison. This showed a similar trend as other curves except that the pore size was below the original level across the total depth of machined sample, i.e., the machining-affected zone was found to persist throughout the

whole sample. In the following sections, the effect of this gradation on compression performance of the foam sample was investigated.

4.2.1. Mechanical Response of Struts

The mechanical performance of the open-cell aluminum foam specimens was investigated using compression tests. The nominal stress-strain curves were obtained from recorded load and displacement values from the compression test and are provided in Figure 4.11. In the case of the unmachined specimen, the stress – strain relation is shown using the blue curve. This response exhibited three main regimes of deformation: (i) an initial linear elastic region from points A-C with a constant modulus of 29.27 MPa calculated from the slope of the linear region and terminating at the plastic collapse stress of 0.70 MPa at the onset of instability at point C, (ii) a plastic collapse plateau region from points C-H up to the strain level of 30% where most of the cells were deformed, and (iii) a densification region from points H-K where sustained deformation resulted in a rapid increase in stress that further compacted the significantly densified microstructure. The initial stress peak and extended stress plateau seen here are well known to be responsible for the excellent energy absorption capacity of such foams.

Similarly, the stress – strain curve for machined specimen, shown in red, exhibited three regions at the same strain levels: (i) a linear elastic region from points A'-C' with a higher constant modulus of 40.65 MPa and a higher yield stress of 1.01 MPa at the

nominal strain of 4% resulting from the local densification along the machined surface, (ii) a plateau region from points C'-H' with higher stresses than that of unmachined specimen, and (iii) a hardening regime from points H'-K' wherein response was consistent with the unmachined specimen from points H-K.

Figure 4.12 and 4.13 summarizes tomographic scans obtained to map the deformation evolution of unmachined and machined specimens as compression progressed. For the unmachined specimen, shown in Figure 4.12, the deformation was macroscopically similar from points A to C (i.e., linear elastic period). From points C to H, struts at the specimen mid-height started to buckle and collapse. Contact between the struts of these buckled unit cells arrested local collapse and caused the deformation to gradually spread to neighboring cells at a nearly constant stress level, this resulting in an initial horizontal crush band covering the entirety of the specimen cross section at point H. In the hardening region, collapsed cells were compacted together and a secondary deformation band formed along the top of sample. Similarly, the machined specimen in Figure 4.13 deformed homogeneously in the linear elastic regime. In the stress plateau region from points C' to H', struts at the specimen mid-height started to collapse and gradually developed an initial failure zone with an inclined angle of 20° with respect to the horizontal direction. In the densification region, a secondary band deformation formed along the top of sample when all struts including those on machined surface had collapsed. A possible explanation for the inclination of the first failure band was the effect of the densified structure in the machined surface, this evident on the right side of each scan in Figure 4.13.

To quantitatively determine the motion of struts in the unmachined sample between successive imaging frames, the inter-frame x-direction, y-direction, z-direction and resultant displacement fields were computed by DVC. These are depicted in Figure 4.14 – 4.17, respectively. In Figure 4.14, the portion of the specimen with non-zero x-direction displacement decreased continually from points A to E, at which point the first deformation band was observed in Figure 4.12. Up to this point, the displacement of the solid was symmetric about the loading axis, with material displacing outward from the centerline of the foam. The inter-frame controlled displacement between successive loading steps was 7 voxels in magnitude, this resulting in a maximum x-directional displacement of 1 voxel as measured by DVC over these loading steps. As the compression progressed, high values of x-direction inter-frame displacements extended from the evolving first deformation band to the secondary deformation band along the top surface of the specimen. The maximum displacement in this deformation band was 3 voxels, while the inter-frame controlled displacement was 10 voxels in magnitude. In Figure 4.15, the y-direction displacement of each loading step as measured by DVC is reported. As in the previous case, the portion of the specimen with non-zero y-direction displacement decreased continually from points A to E. For subsequent loading points, the maximum y-direction inter-frame displacement was also 3 voxels.

The z-direction inter-frame displacement field, shown in Figure 4.16, had a markedly different appearance. For these fields, a graded displacement pattern existed from the bottom to the top, as the bottom plate was moving relative to the stationary top plate. The interface between the zero and non-zero portions of the displacement field provides

an indication of the location of the initial deformation band. From points F to J, regions of the specimen indicating non-zero z-direction displacement extended to the secondary deformation band along the top of the specimen, this initiating at point H at the interface between the zero and non-zero portions of the displacement field. The z-directional displacement had a dominant contribution to the resultant inter-frame displacement field, which is shown in Figure 4.17 to be similar to the z-direction displacement field of Figure 4.16.

From the displacement fields for the unmachined specimen, inter-frame strain fields were evaluated and are provided in Figure 4.18 – 4.24. At the initial stages of the deformation, the maximum incremental ε_{xx} strain was 2% throughout the entire solid, as shown in Figure 4.18. As deformation continued from points A to E, deformation localized near initiation site of the first deformation band, as in Figure 4.14. At later stages of deformation, high values of incremental strain up to 10% occurred at the secondary band zone along the top surface, this observed at points H and I. Similar behavior was observed for the evolution of the incremental ε_{yy} strain in Figure 4.19. To investigate the normal strain field along the loading direction, Figure 4.20 shows the incremental ε_{zz} strain field for each compression step. From points A to E, the portion of the specimen undergoing deformation had a uniform strain value of -2%, this consistent with the heterogeneity observed in Figure 4.16 for z-direction displacement. From points G to I, large strains of -10% were found to persist in the top and bottom of the specimen, indicating the formation of a secondary deformation band.

Figure 4.21 – 4.23 summarizes the evolution of the shear strain fields at each loading step in the compression process. In Figure 4.21, a maximum value of γ_{xy} = 2% occurred in the vicinity of the deformation band zone from points A to E, this suggesting that the shear component of the deformation on the x-y plane contributed to the deformation band formation as well as that of the normal strains. From points F to J, the γ_{xy} shear strain field had a uniform distribution across the whole sample with magnitude between 0% and 2%, except for a small region exhibiting 10% incremental strain in the secondary band zone at point H. Similarly, the γ_{yz} strain field in Figure 4.22 and the γ_{zx} strain field in Figure 4.23 exhibited a similar distribution pattern as that of Figure 4.21. The incremental effective strain fields for each point in the compression process are plotted in Figure 4.24. As discussed above on each strain component.

In a manner similar to the above for the unmachined sample, Figure 4.25 – 4.28 and Figure 4.29 – 4.35 were generated to quantify the displacement and strain fields of struts in the machined sample. In general, each of these fields showed formation of a deformation band inclined at an angle of 20° from horizontal orientation, this consistent with the observations of deformation in Figure 4.13. From Figure 4.25, the x-direction displacement field exhibited markedly different response than the unmachined sample, with the central portion of the foam moving leftward in the image and the top/bottom of the foam moving to rightward. The main reason for this redistribution relative to the unmachined sample was the shielding effect of the local densification along the machined surface. At points D' and E', the shielding effect started to vanish because of

local collapse on the machined surface, resulting formation of the inclined deformation band formation. For the following loading steps, the specimen behaved similarly to the unmachined specimen in Figure 4.14, especially in terms of the secondary deformation band formation along the top surface. The discrepancy in localized deformation response is a plausible source of the difference between the measured stress-strain curves of the unmachined and machined samples from points A to H and A' to H'. Further, the similarity in the deformation response beyond these points is consistent with the similarity in stress-strain response as well.

Similar to that in Figure 4.16, the inter-frame z-direction displacement in Figure 4.27, decreased from 7 voxels to 0 voxels from points A' to E', with the formation of an inclined deformation band. Once again, the non-zero portion of the z-direction displacement field extended to the potential secondary deformation band for subsequent points, consistent with the behavior observed Figure 4.25 and 4.26. The presence of a thin layer along the machined surface with near-zero displacement from points A' to C', indicated the shielding effect resulting from the existence of machined surface. The incremental resultant displacement field shown in Figure 4.28 closely resembled the z-direction displacement field of Figure 4.27, as the z-directional displacement was the primary contributor to the resultant inter-frame displacement.

For the inter-frame strain fields shown in Figure 4.29 – 4.35, the distributions were almost the same as in the unmachined foam behavior in Figure 4.18 – 4.24, except for the formation of the inclined deformation band. In Figure 4.29 and 4.30, maximum

incremental ε_{xx} and ε_{yy} strains of 2%, were distributed uniformly throughout the specimen at points A' and B', this eventually localizing to the location of the first deformation band. For points F' to J', regions with strain levels of 10% extended to the secondary band zone at the top of the specimen. For the shear components, the γ_{xy} component contributed significantly to the deformation band formation from stage A' to E' in Figure 4.32. From points F' to J', γ_{xy} was distributed homogeneously across the whole specimen with the magnitude from 0% to 2%, except that incremental strains in excess of 10% occurred in the vicinity of the secondary band zone. The same conclusion could be drawn from Figure 4.33 and 4.34, for the γ_{yz} and γ_{zx} components. In this particular case, all strain components contributed equally to the incremental effective strain field shown in Figure 4.35.

4.2.2. Pore Morphological Evolution during Compression Tests

To determine evolution of the pore-phase structure during the compression tests, watershed segmentation was employed to characterize the pore morphologies for both unmachined and machined specimens. It was observed that, pores decreased continuously in size and their shapes changed gradually with increasing compressive strain. In Figure 4.36, the evolution of select pores were plotted with the strut network for each loading step on the unmachined sample. From the figure, the pore morphology did not change significantly from points A to C, this corresponding to the linear elastic region in Figure 4.11. From point C onward, the pores located close to the specimen

mid-height deformed due to the formation of the localized deformation band, this resulting in a decrease of the pore size. Afterwards, particularly beyond point H, the unit cells shrank in size across the whole sample and the nominal pore diameter dropped below 1 mm, corresponding to the dark color in the figure. For the machined sample, a similar change of pore size and morphology could be observed in Figure 4.37, especially along the band formation zones. In comparison with the unmachined sample, pores with dark color (i.e., small diameters) showed up nearly one step later in the deformation sequence. This data supports the notion of a strengthening effect from the machined layer.

To quantitatively evaluate the pore size distribution, histograms of pore diameter were generated in Figure 4.38 for both samples. In general, the data appeared to follow a Gaussian distribution at the very first compressive steps. As the uniaxial loading continued, the peak of the distribution shifted towards small pore diameters, as the typical diameter decayed from 3.2 mm to 0.3 mm. This resulted in a log-normal type distribution at the last two loading steps in the compression test. Simultaneously, the number of pores rose steeply in these final stages of deformation. This observation could be explained by the occurrence of pore division resulting from the full collapse and densification of the cellular metal foam. In addition, the machining process likely caused local smearing on the machined surface and correspondingly the formation of smaller local pore diameters in the near surface region, as shown in Figure 4.38 for every loading step.

4.2.3 Discussion

To further understand the deformation mechanisms of graded open-cell foams, the compressive mechanical properties can be modeled based on the well-established Gibson-Ashby scaling law: $\frac{\sigma_{pl}}{\sigma_s} = C\left(\frac{\rho}{\rho_s}\right)^n$, where σ_{pl} and ρ represent the plastic collapse stress and initial density of the foam, while σ_s and ρ_s the yield stress and density of the parent metal [55]. The constants C and n indicate structure dependent parameter and scaling exponent. Following this equation, the relation between unmachined sample and machined surface is given by $\frac{\sigma_{pl}^2}{\sigma_{pl}^1} = K\left(\frac{\rho^2}{\rho^1}\right)^n$, where unmachined sample is marked by the subscript 1, while the machined surface by the subscript 2, and the constant $K = \frac{C_2}{C_1}$. Prior to constructing the model, three assumptions are made: (1) the relation formulated by the scaling law can be extended to high strain region (i.e., σ_{pl} represents flow stress [4]); (2) strain dependence is added to both σ_{pl} and ρ (i.e., the relation becomes $\frac{\sigma_{pl}^2(\varepsilon)}{\sigma_{pl}^1(\varepsilon)} = K\left(\frac{\rho^2(\varepsilon)}{\rho^1(\varepsilon)}\right)^n$); (3) for the machined sample, or the combination of machined surface and part of unmachined sample, the iso-strain model is satisfied, and the two different sections are non-interacting. The justification for the last assumption is that the shielding effect mainly operates in the linear elastic region, verified by the displacement fields of the machined specimen in Figure 4.25 – 4.28.

Based on the assumptions made above, the true stress versus true strain relations for both samples are evaluated from Figure 4.11, and shown in Figure 4.39(a). To quantify the relative density at each loading step, the solid volume fraction was calculated by voxel counting on the thresholded binary images, and the relative density evolution

profiles for both specimens are shown in Figure 4.39(b). The latter two assumptions of this model implies that the total true stress σ as a function of true strain ε can be determined by:

$$\sigma(\varepsilon) = \sigma_1(1-p) + \sigma_2 p = \sigma_1(\varepsilon)(1-p) + K\sigma_1(\varepsilon)\left(\frac{\rho_2(\varepsilon)}{\rho_1(\varepsilon)}\right)^n p$$

where the volume fraction of the smeared machined surface $p = 0.3$, determined by the solid volume fraction profile along the x-axis at the initial compressive step A'. Since $\sigma(\varepsilon)$ and $\sigma_1(\varepsilon)$ are given in Figure 4.39(a), and $\frac{\rho_2(\varepsilon)}{\rho_1(\varepsilon)}$ can be determined by Figure 4.39(b), the unknown constants K and n are computed by logarithmic least squares method. Figure 4.39(c) provides the fitted model for the machined sample, where $K = 0.91$ and $n = 5.14$. This value of K indicates a slight decrease of C_2 compared with C_1, and this can be explained by the imperfect structure caused by the machining process. In addition, a lower value of K represents less mechanical efficient struts experiencing buckling and plastic collapse [4]. The high value of n results from the assumption of the strain dependence of stress and density, especially in the densification region. In the future, more experiments would be conducted to verify this model.

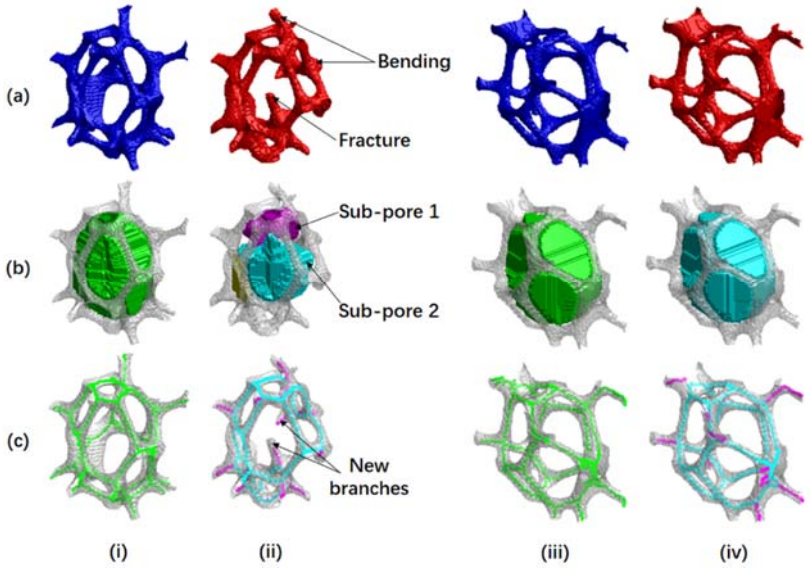

Figure 4.1. Initial and final structure for v_c = 2.6 m/s, v_f = 0.204 mm/min, a_p = 1.5 mm, including: (a) reconstructed model, (b) segmented pores and (c) medial axis extracted for cells at various depths from the machined surface: (i) d = 1.5 mm (initial), (ii) d = 1.5 mm (post-machined), (iii) d = 8.5 mm (initial), (iv) d = 8.5 mm (post-machined).

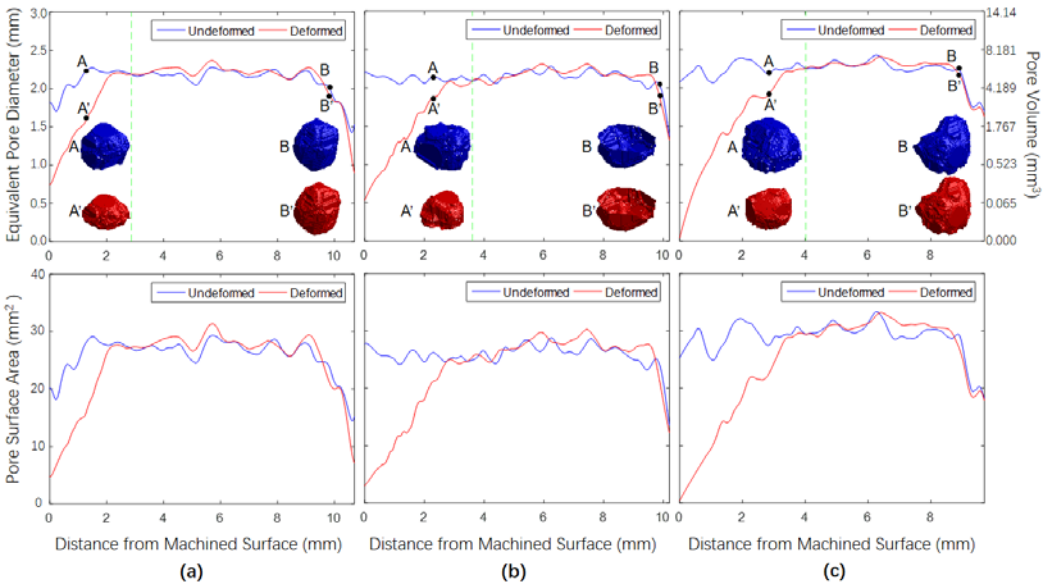

Figure 4.2. Pore diameter and surface area as a function of distance from the machined surface for foams machined under experimental conditions (a) v_c = 2.6 m/s, v_f = 0.051 mm/min, a_p = 1.0 mm, (b) v_c = 2.6 m/s, v_f = 0.051 mm/min, a_p = 1.5 mm, (c) v_c = 2.6 m/s, v_f = 0.051 mm/min, a_p = 2.0 mm.

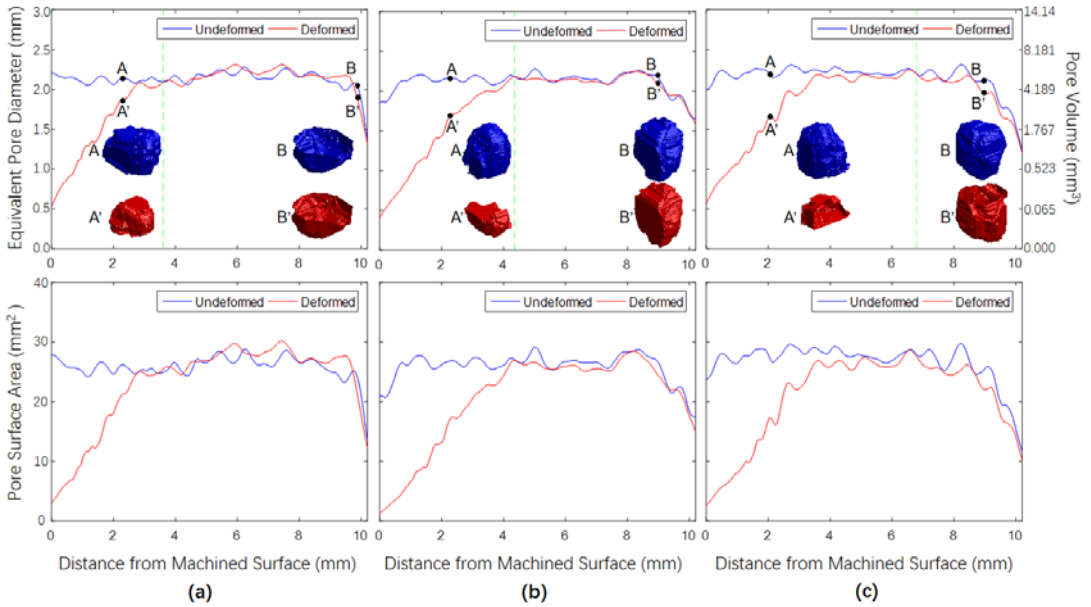

Figure 4.3. Pore diameter and surface area as a function of distance from the machined surface for foams machined under experimental conditions (a) v_c = 2.6 m/s, v_f = 0.051 mm/min, a_p = 1.5 mm, (b) v_c = 2.6 m/s, v_f = 0.102 mm/min, a_p = 1.5 mm, (c) v_c = 2.6 m/s, v_f = 0.204 mm/min, a_p = 1.5 mm.

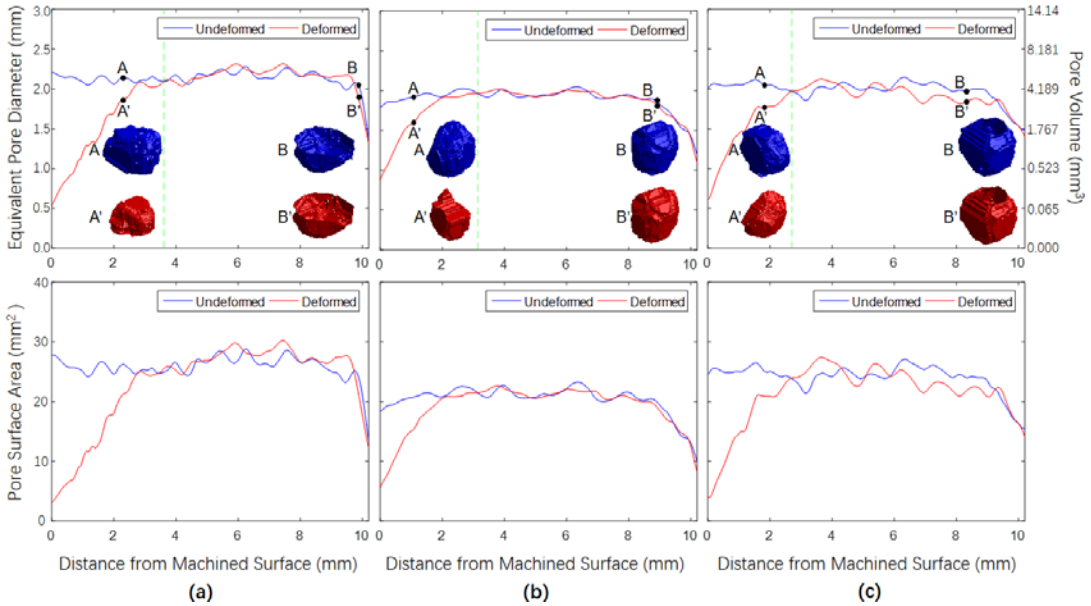

Figure 4.4. Pore diameter and surface area as a function of distance from the machined surface for foams machined under experimental conditions (a) v_c = 2.6 m/s, v_f = 0.051 mm/min, a_p = 1.5 mm, (b) v_c = 3.7 m/s, v_f = 0.051 mm/min, a_p = 1.5 mm, (c) v_c = 5.2 m/s, v_f = 0.051 mm/min, a_p = 1.5 mm.

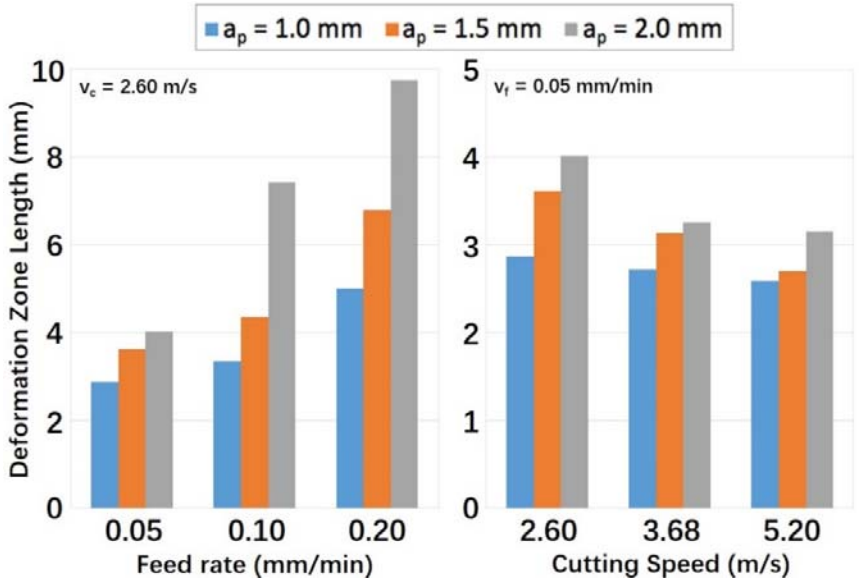

Figure 4.5. Effects of feed rate and cutting speed on deformation zone size for various depths of cut.

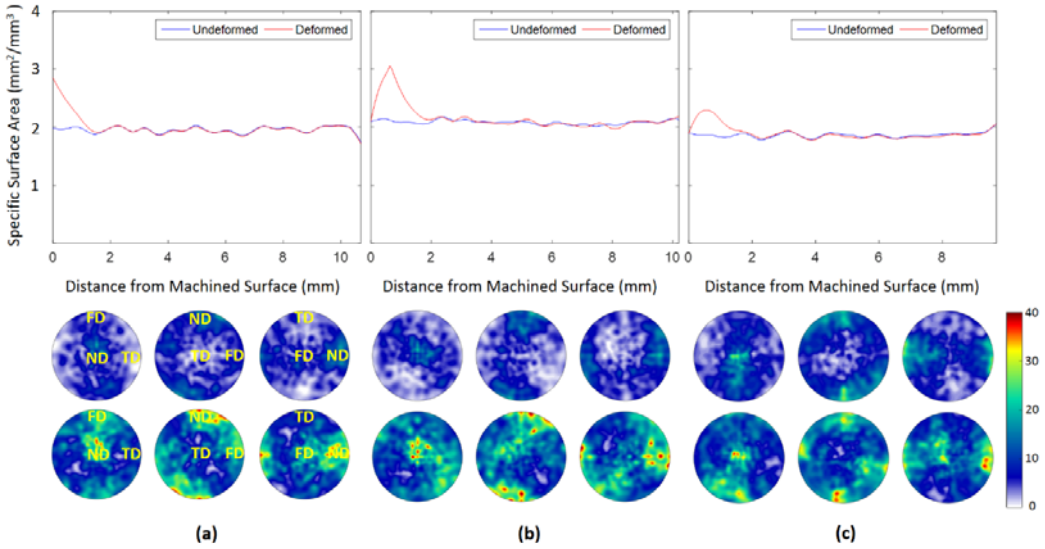

Figure 4.6. Specific strut surface area as a function of distance from the machined surface for foams machined under experimental conditions (a) v_c = 2.6 m/s, v_f = 0.051 mm/min, a_p = 1.0 mm, (b) v_c = 2.6 m/s, v_f = 0.051 mm/min, a_p = 1.5 mm, (c) v_c = 2.6 m/s, v_f = 0.051 mm/min, a_p = 2.0 mm, with corresponding strut branch orientation density variations in original samples (upper part) and machined samples (lower part).

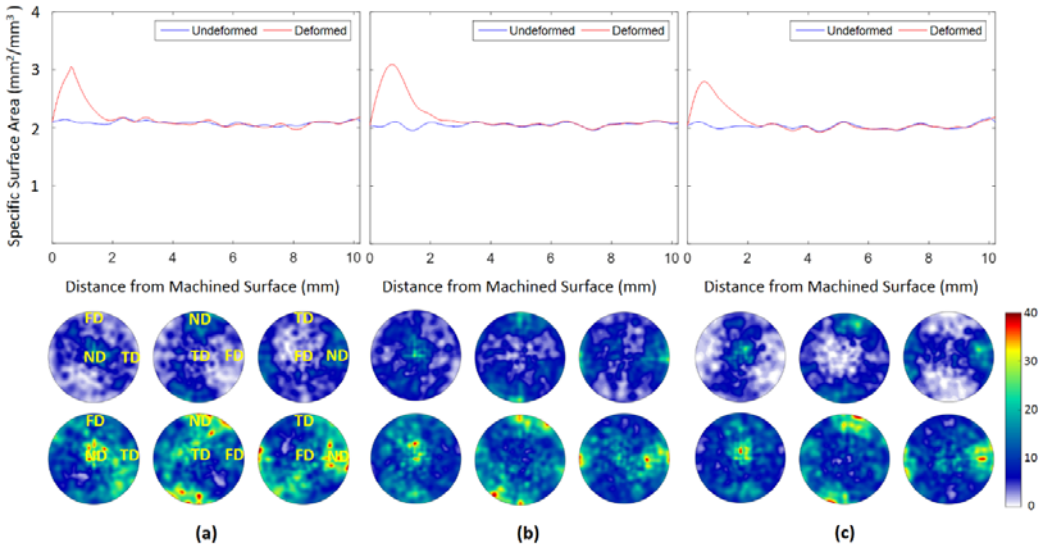

Figure 4.7. Specific strut surface area as a function of distance from the machined surface for foams machined under experimental conditions (a) v_c = 2.6 m/s, v_f = 0.051 mm/min, a_p = 1.5 mm, (b) v_c = 2.6 m/s, v_f = 0.102 mm/min, a_p = 1.5 mm, (c) v_c = 2.6 m/s, v_f = 0.204 mm/min, a_p = 1.5 mm, with corresponding strut branch orientation density variations in original samples (upper part) and machined samples (lower part).

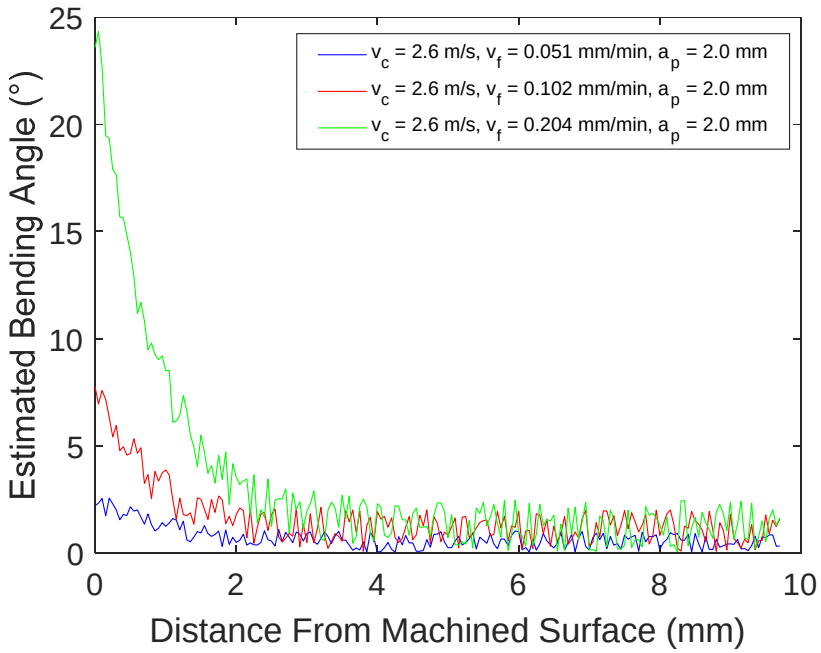

Figure 4.8. Measured strut bending angle as a function of distance from the machined surface for foams machined at increasing feed rate.

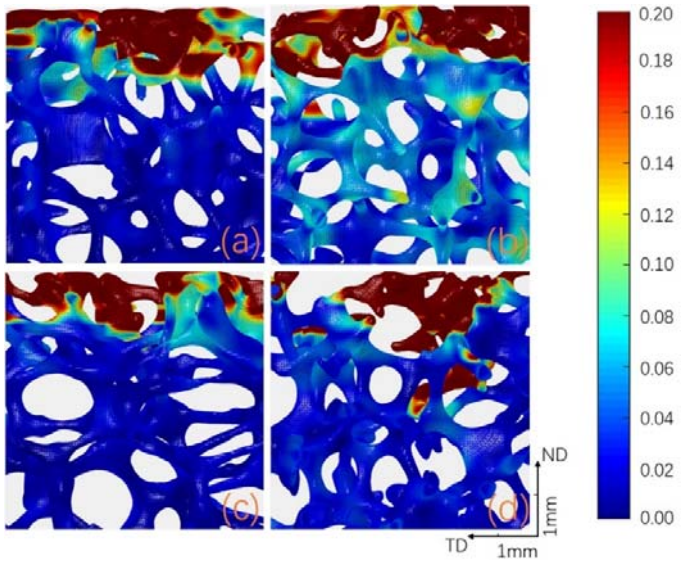

Figure 4.9. Subsurface strain distribution from digital volume correlation of initial and post-machined samples at a constant v_c = 2.6 m/s, feed rates of (a, c) v_f = 0.102 mm/min and (b, d) v_f = 0.204 mm/min, axial depths of cut of (a, b) a_p = 1.5 mm and (c, d) a_p = 1.0 mm.

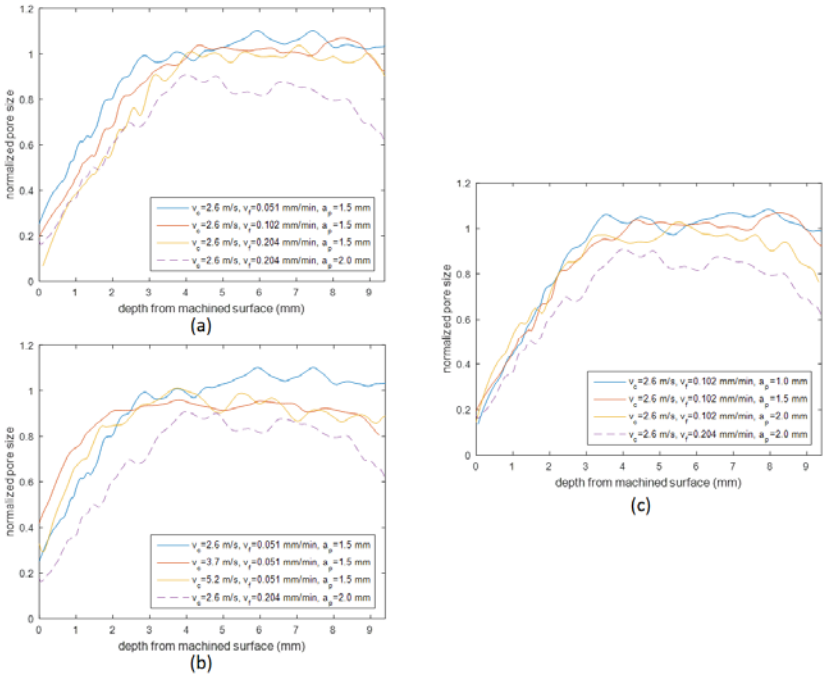

Figure 4.10. Pore size profile along the depth from machined surface under (a) various feed rates, (b) various cutting speeds and (c) various depths of cut.

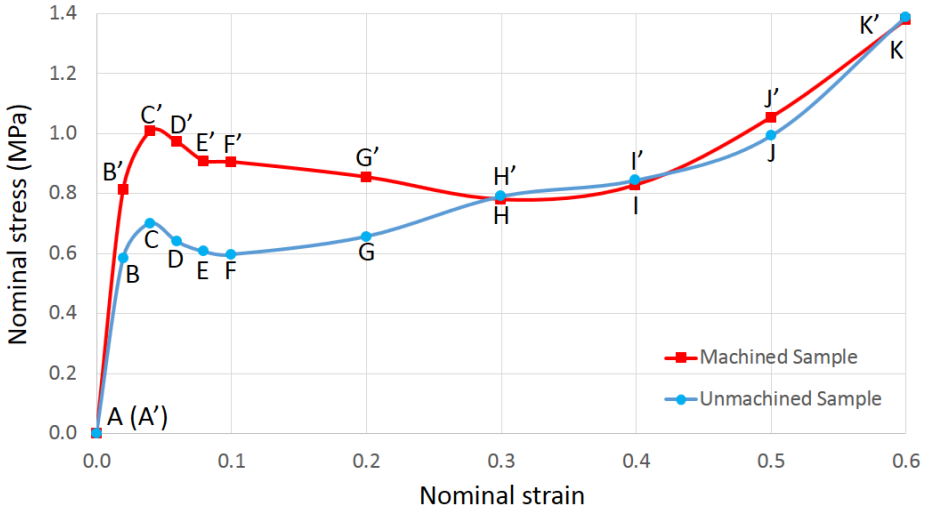

Figure 4.11. Stress-strain curves in compressions of specimens extracted from unmachined and machined samples respectively.

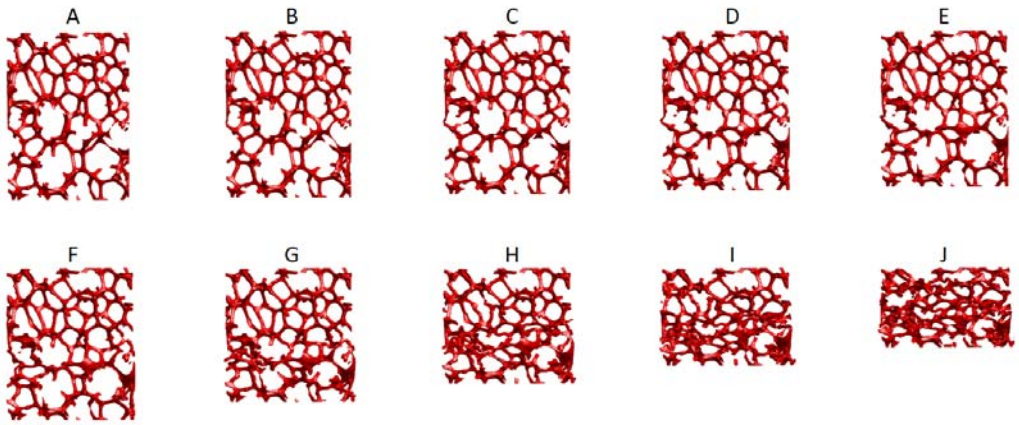

Figure 4.12. Deformed configurations of the unmachined specimen corresponding to states shown in Figure 4.11.

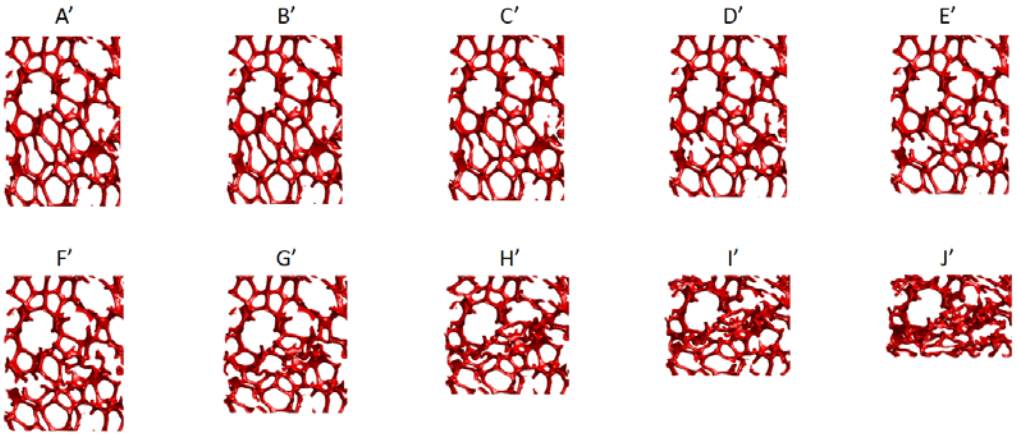

Figure 4.13. Deformed configurations of the machined specimen corresponding to states shown in Figure 4.11.

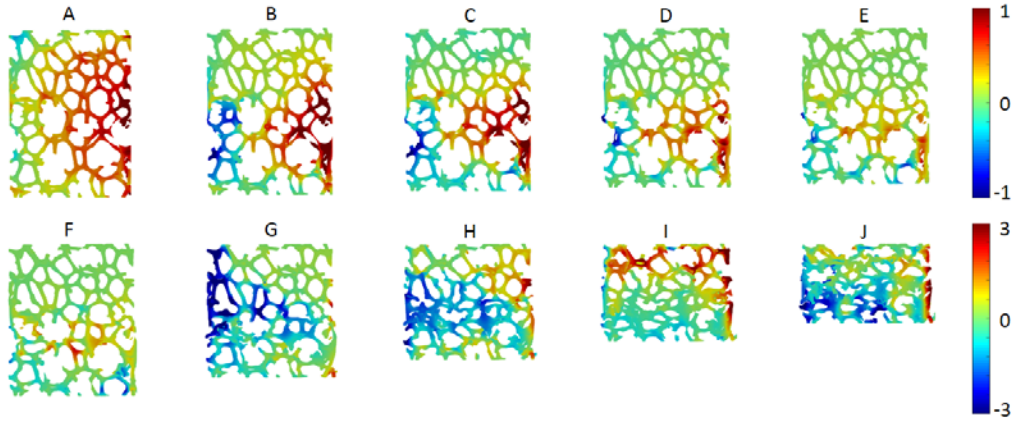

Figure 4.14. Incremental x-directional (positive to the right) displacement component (in the unit of voxel) for each configuration of the unmachined specimen.

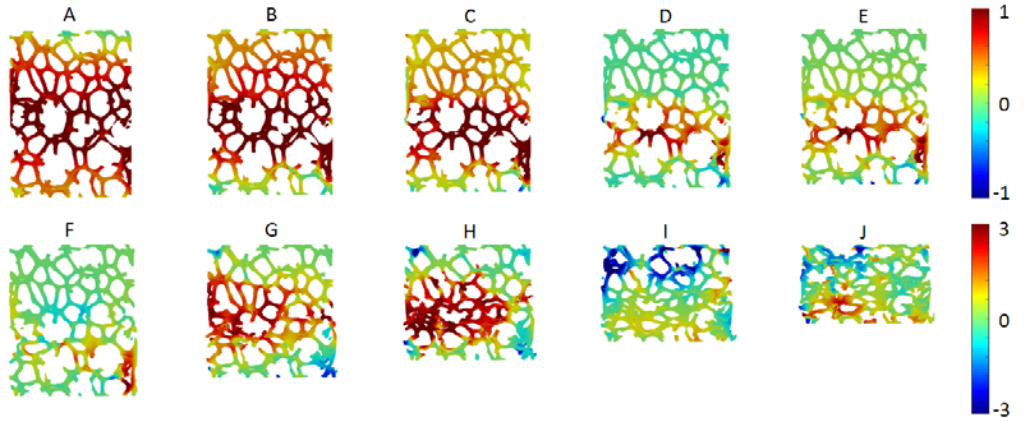

Figure 4.15. Incremental y-directional (positive into the page) displacement component (in the unit of voxel) for each configuration of the unmachined specimen.

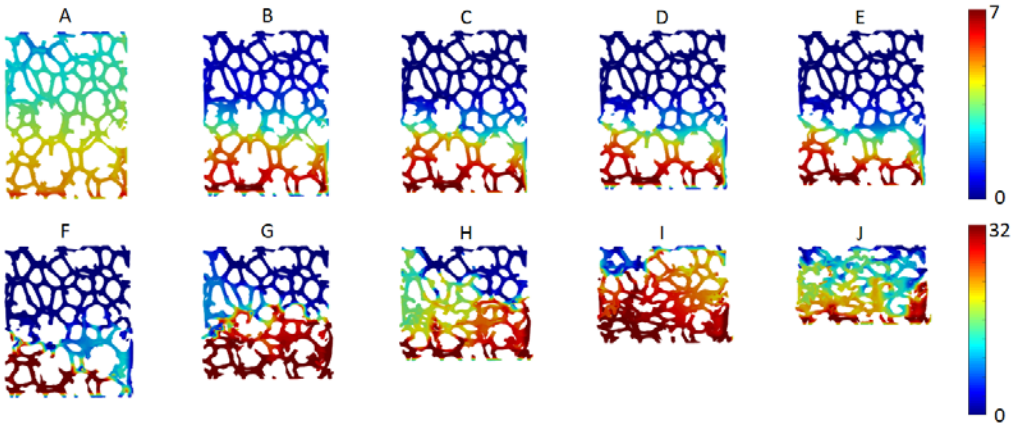

Figure 4.16. Incremental z-directional (positive to the upwards) displacement component (in the unit of voxel) for each configuration of the unmachined specimen.

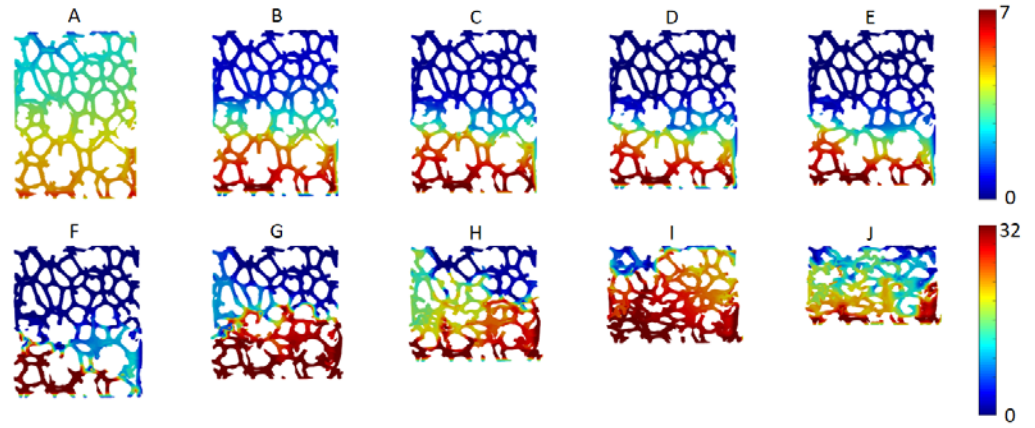

Figure 4.17. Incremental resultant displacement (in the unit of voxel) for each configuration of the unmachined specimen.

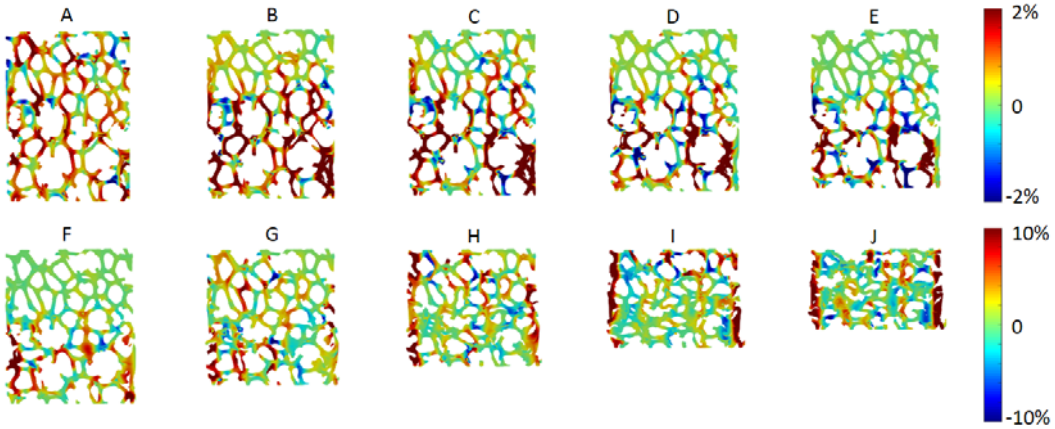

Figure 4.18. Incremental ε_{xx} for each configuration of the unmachined specimen.

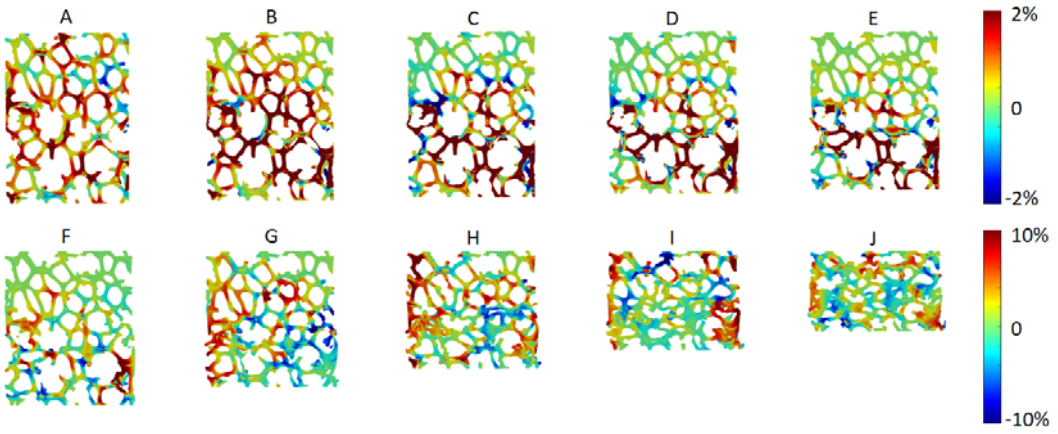

Figure 4.19. Incremental ε_{yy} for each configuration of the unmachined specimen.

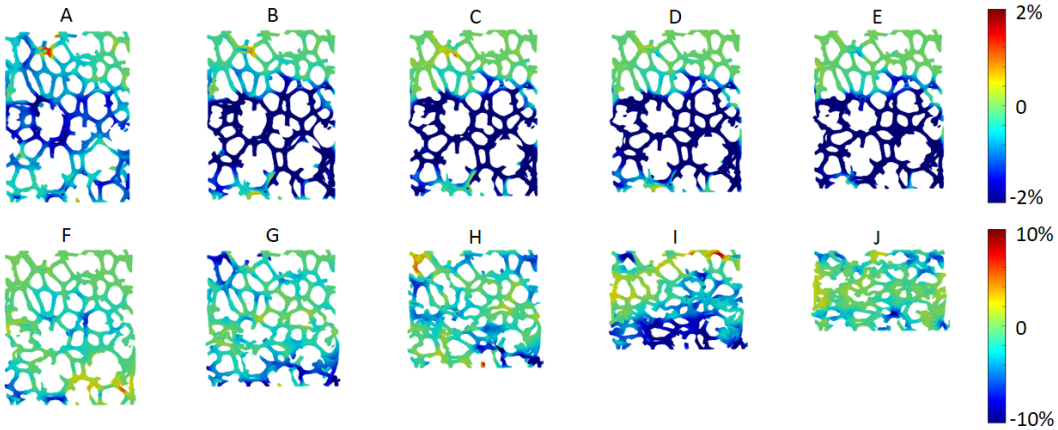

Figure 4.20. Incremental ε_{zz} for each configuration of the unmachined specimen.

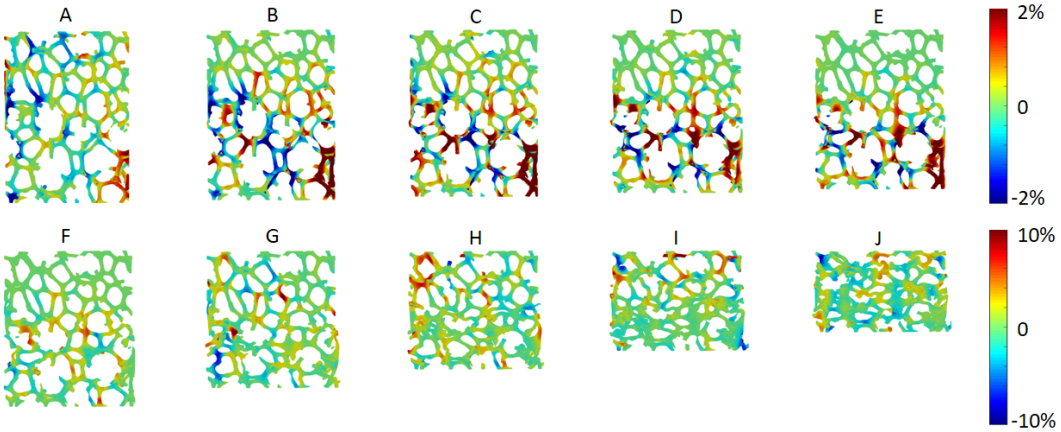

Figure 4.21. Incremental γ_{xy} for each configuration of the unmachined specimen.

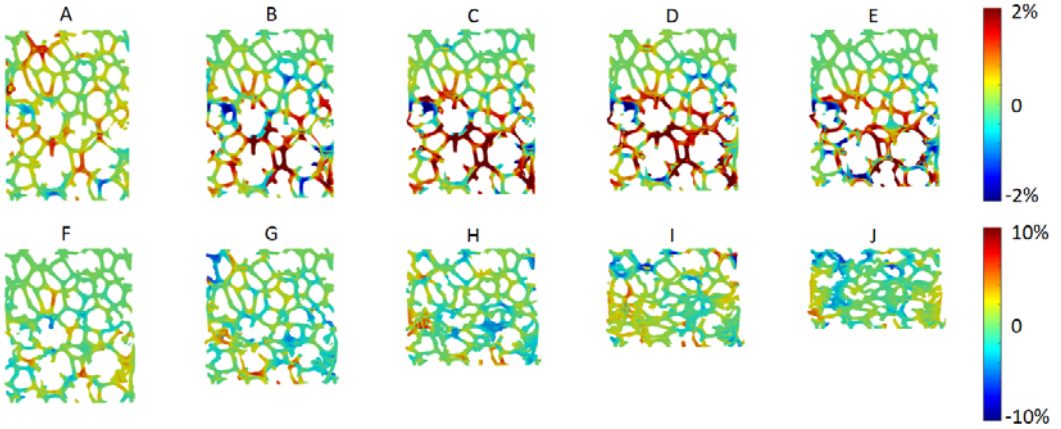

Figure 4.22. Incremental γ_{yz} for each configuration of the unmachined specimen.

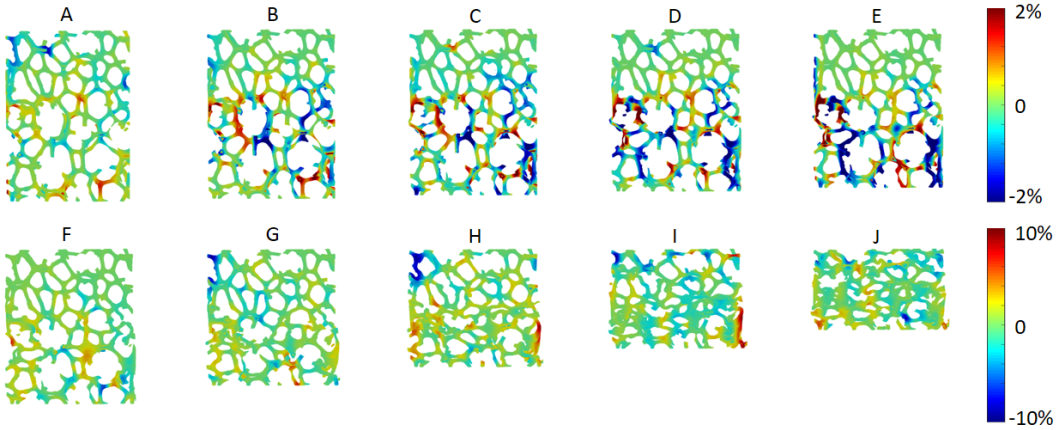

Figure 4.23. Incremental γ_{zx} for each configuration of the unmachined specimen.

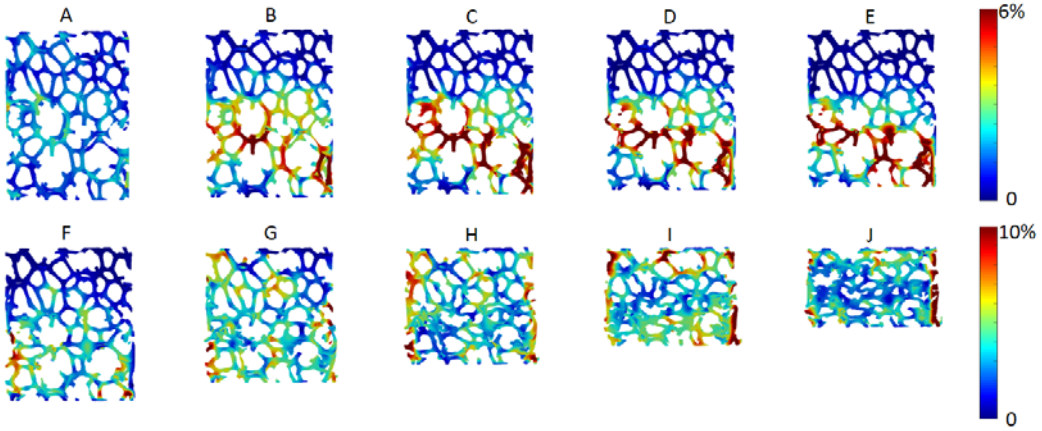

Figure 4.24. Incremental effective strain for each configuration of the unmachined specimen.

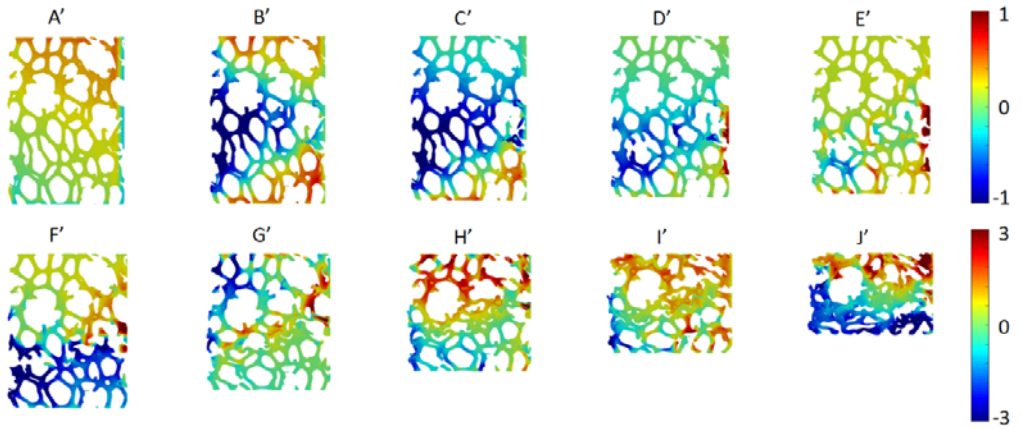

Figure 4.25. Incremental x-directional (positive to the right) displacement component (in the unit of voxel) for each configuration of the machined specimen.

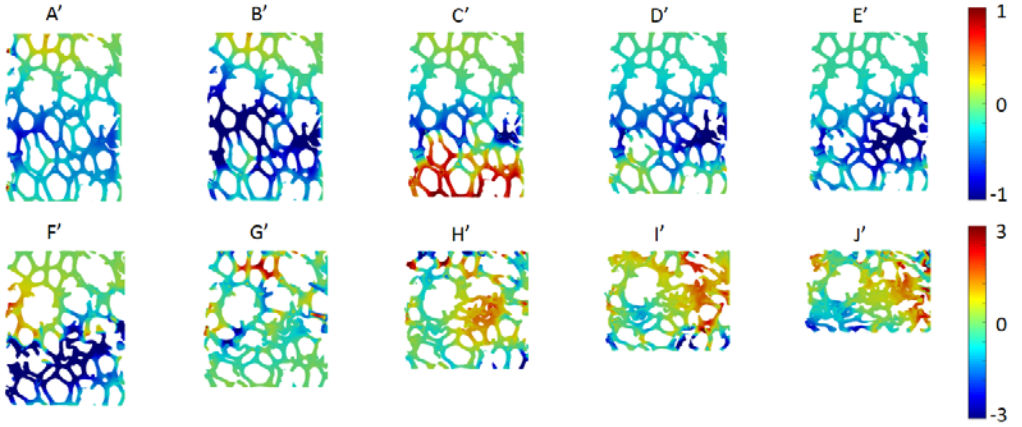

Figure 4.26. Incremental y-directional (positive into the page) displacement component (in the unit of voxel) for each configuration of the machined specimen.

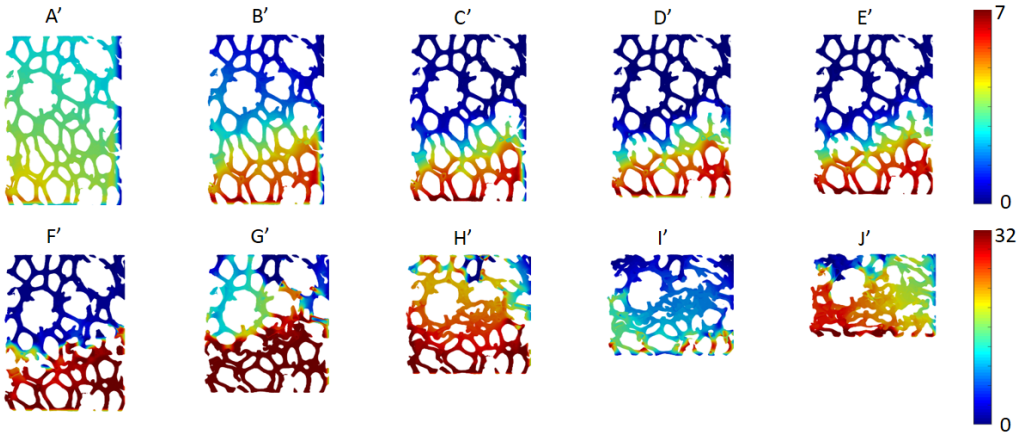

Figure 4.27. Incremental z-directional (positive to the upwards) displacement component (in the unit of voxel) for each configuration of the machined specimen.

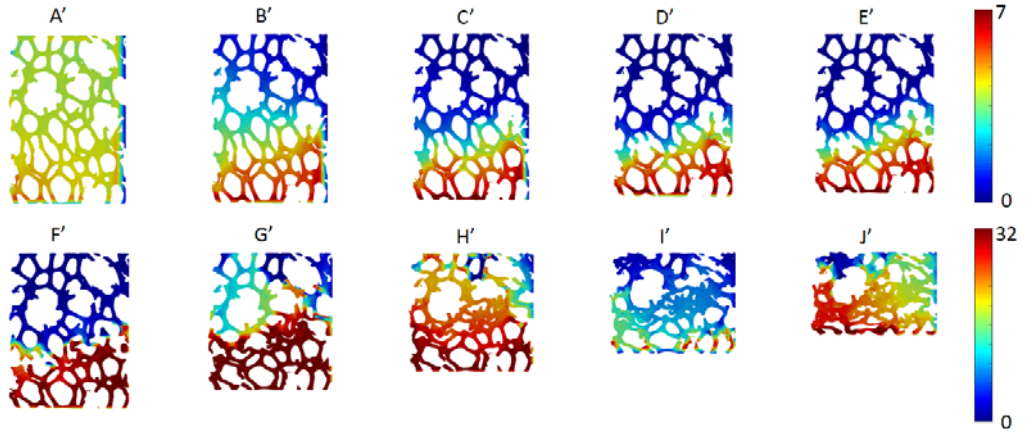

Figure 4.28. Incremental resultant displacement (in the unit of voxel) for each configuration of the machined specimen.

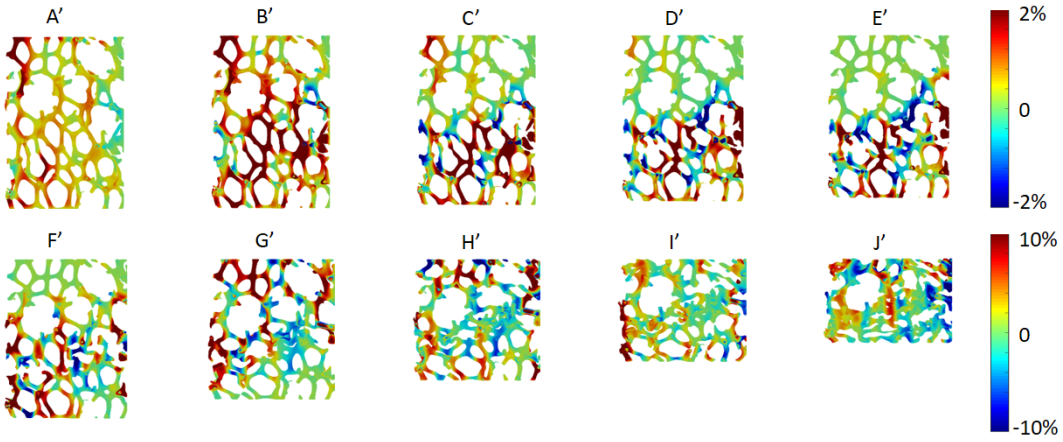

Figure 4.29. Incremental ε_{xx} for each configuration of the machined specimen.

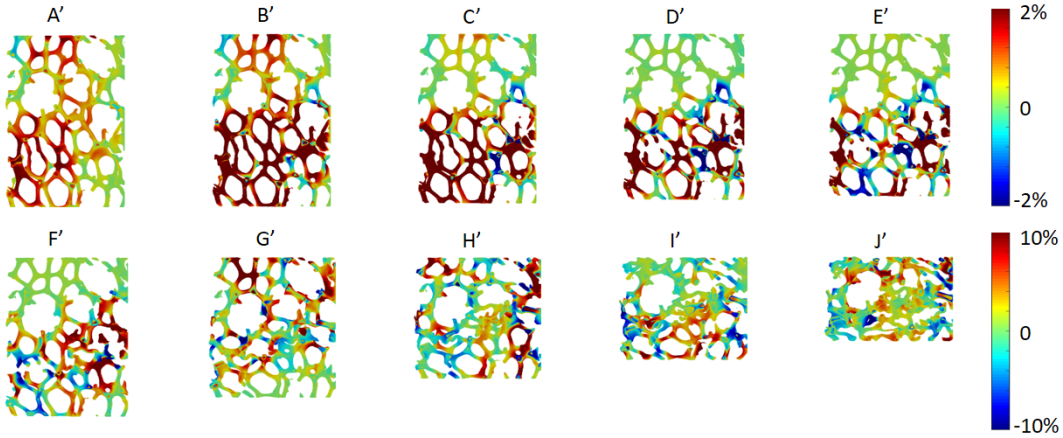

Figure 4.30. Incremental ε_{yy} for each configuration of the machined specimen.

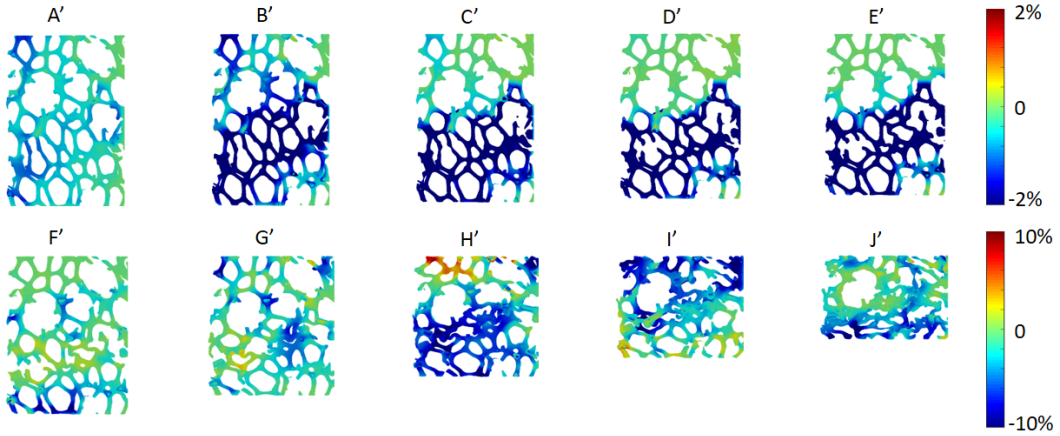

Figure 4.31. Incremental ε_{zz} for each configuration of the machined specimen.

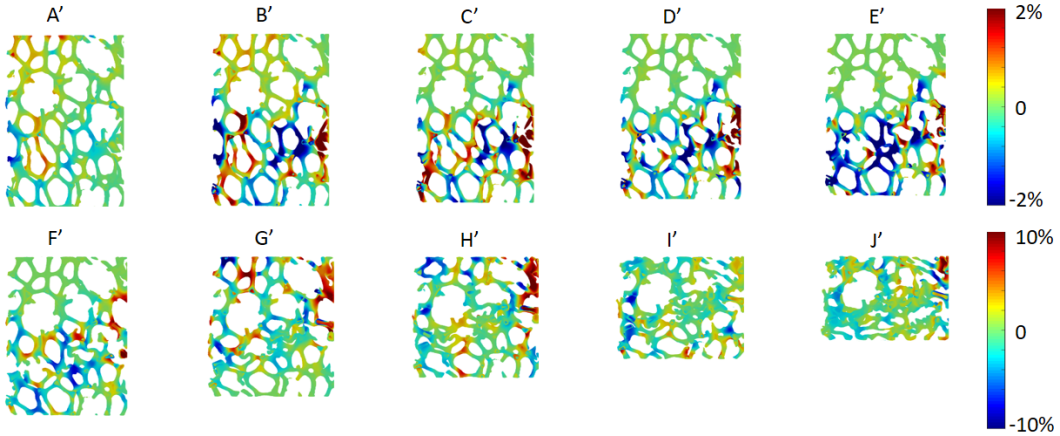

Figure 4.32. Incremental γ_{xy} for each configuration of the machined specimen.

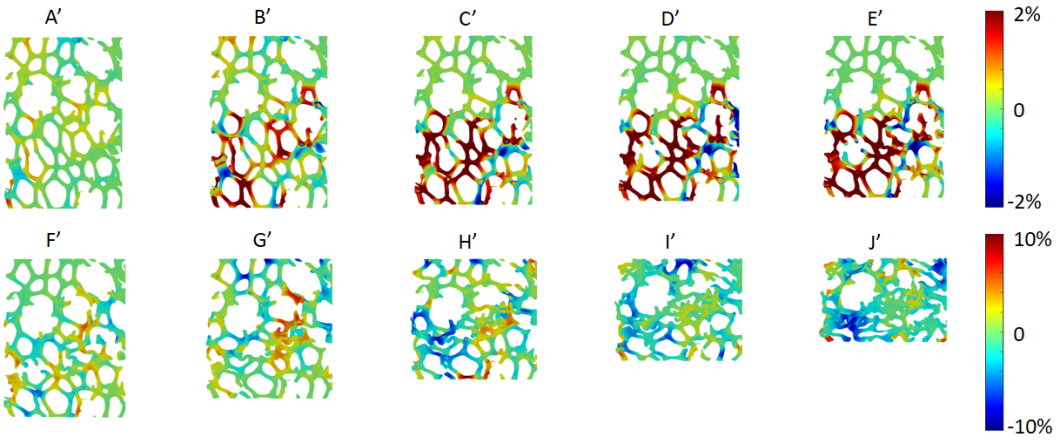

Figure 4.33. Incremental γ_{yz} for each configuration of the machined specimen.

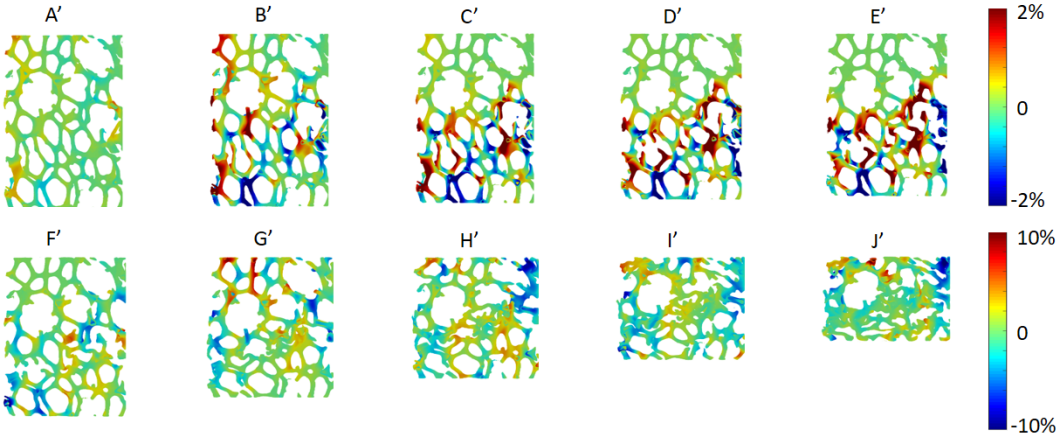

Figure 4.34. Incremental γ_{zx} for each configuration of the machined specimen.

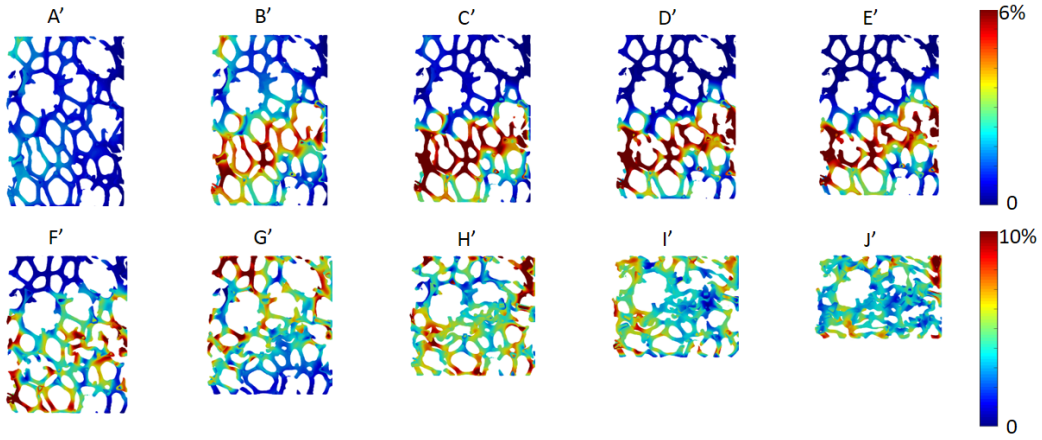

Figure 4.35. Incremental effective strain for each configuration of the machined specimen.

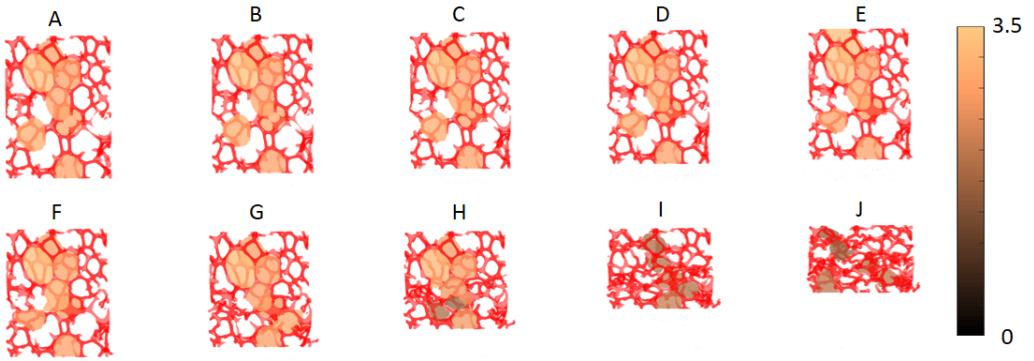

Figure 4.36. Pore size (in the unit of mm) and morphological evolution of the unmachined specimen corresponding to states shown in Figure 4.11.

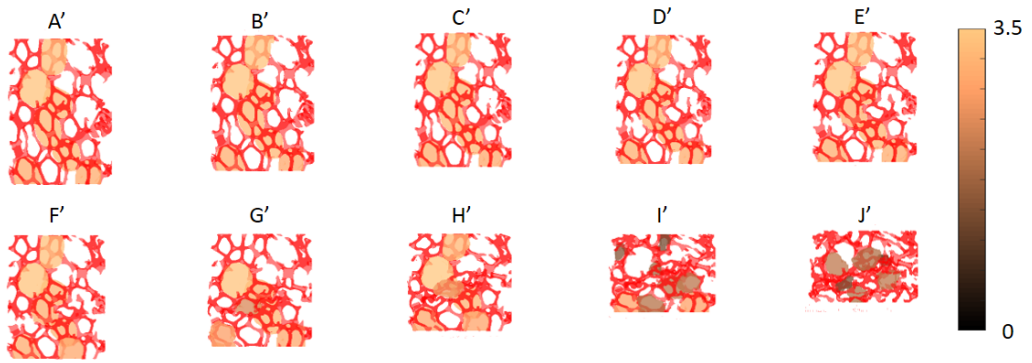

Figure 37. Pore size (in the unit of mm) and morphological evolution of the machined specimen corresponding to states shown in Figure 4.11.

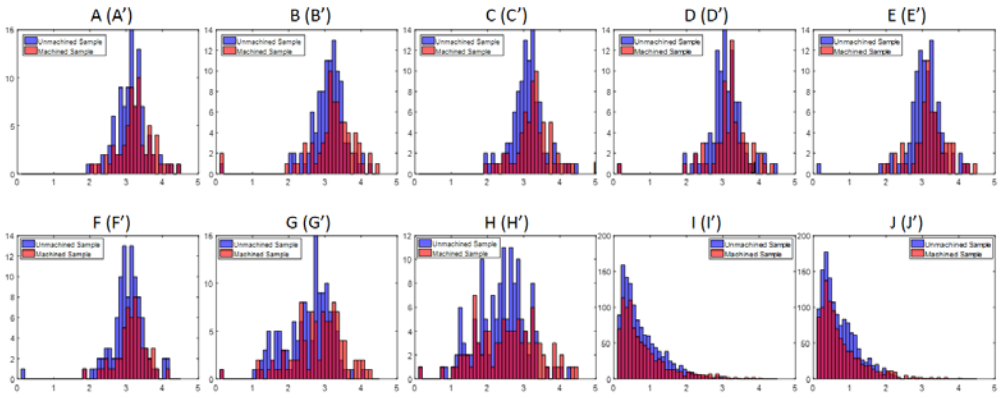

Figure 4.38. Histograms of equivalent pore diameter of the unmachined and machined specimens corresponding to states shown in Figure 4.11.

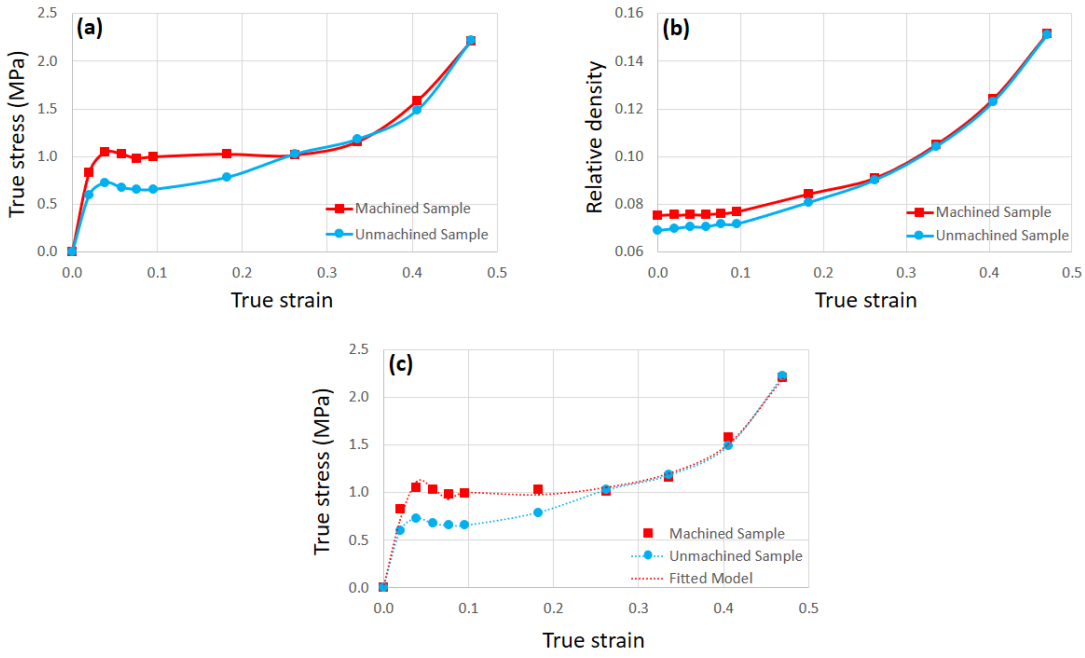

Figure 4.39. (a) the true stress – true strain curves, (b) the relative density evolution profiles with true strain, and (c) fitted model for the machined sample accompanied by the data in (a).

CHAPTER 5. CONCLUSIONS AND FUTURE WORK

In the present study, X-ray micro-computed tomography was utilized to characterize the surface integrity in cellular solids processed by machining, and facilitated evaluating the effect of the structural gradation on mechanical response through *in situ* compression tests. A MATLAB-based pore and strut network analysis algorithms were utilized to investigate the effects of machining parameters on elements of surface integrity, in terms of changes in effective pore size and deformations measured in the solid strut network. Estimation of the subsurface deformation zone by measurements of decrease in effective pore size indicated that the size of the deformation-affected layer was most strongly affected by feed rate and axial depth of cut, with a less significant contribution due to cutting speed. The size of the deformation zone ranged from 1 to 4 times the initial pore/cell diameter, depending on the machining conditions selected. The deformation zone size increased with increasing feed rate and/or axial depth of cut, but decreased with increasing cutting speed. Measurement of both strut deformations and visualizations of subsurface strain distributions indicated similar effects, with a maximum strain of 20% measured in the deformed subsurface.

To quantify the deformation field on the strut level, digital volume correlation was implemented with major uncertainties from mechanical perturbation in the CT machine. The resulting stress – strain curves include three typical regions: (i) a linear elastic region, (ii) an extended stress plateau region and (iii) a final densification region. The

primary effects of machining processes include a local densification along the machined surface causing enhanced stiffness and plastic collapse stress at low strains, and a shielding effect resulting in an inclined crush zone. An extended Gibson-Ashby model was briefly discussed to provide a further understanding of the density gradient effect.

Future experiments will be performed to study the deformation mechanisms during machining-based processing and compressive loading. In addition, it will be interesting to investigate the effects of the foam subsurface damage on mechanical and biointegration performance. This will play a key role in linking application performance measures to quality measures of interest.

REFERENCES

1. Wadley, H.N., *Cellular metals manufacturing.* Advanced Engineering Materials, 2002. **4**(10): p. 726-733.
2. DaviesGJ, S., *Review MetallicFoams: TheirProduction, PropertiesandApplications.* J MaterialScience, 1983. **18**(1): p. 1899-1908.
3. Murr, L.E., et al., *Next-generation biomedical implants using additive manufacturing of complex, cellular and functional mesh arrays.* Philos Trans A Math Phys Eng Sci, 2010. **368**(1917): p. 1999-2032.
4. Brothers, A.H. and D.C. Dunand, *Mechanical properties of a density-graded replicated aluminum foam.* Materials Science and Engineering: A, 2008. **489**(1-2): p. 439-443.
5. Hangai, Y., et al., *Nondestructive observation of pore structure deformation behavior of functionally graded aluminum foam by X-ray computed tomography.* Materials Science and Engineering: A, 2012. **556**: p. 678-684.
6. Cui, L., S. Kiernan, and M.D. Gilchrist, *Designing the energy absorption capacity of functionally graded foam materials.* Materials Science and Engineering: A, 2009. **507**(1-2): p. 215-225.
7. Conde, Y., A. Pollien, and A. Mortensen, *Functional grading of metal foam cores for yield-limited lightweight sandwich beams.* Scripta Materialia, 2006. **54**(4): p. 539-543.
8. Togashi, H., K. Yuki, and H. Hashizume, *Heat transfer enhancement technique with copper fiber porous media.* Fusion science and technology, 2005. **47**(3): p. 740-745.
9. Matsumoto, Y., et al., *Uniform and graded chemical milling of aluminum foams.* Materials Science and Engineering: A, 2007. **447**(1-2): p. 150-157.
10. Neubrand, A., *Electrochemical processing of porosity gradients for the production of functionally graded materials.* Journal of applied electrochemistry, 1998. **28**(11): p. 1179-1188.
11. Solaiyan, C., et al., *Preparation and characterisation of porous electrodes from nickel powder for fuel cells.* 1999.
12. Song, Z., S. Kishimoto, and N. Shinya, *A Novel Pulse-Current-Assisted Sintering Method for Fabrication of Metallic Cellular Structures.* Advanced Engineering Materials, 2004. **6**(4): p. 211-214.
13. Hangai, Y., et al., *Fabrication of functionally graded aluminum foam using aluminum alloy die castings by friction stir processing.* Materials Science and Engineering: A, 2012. **534**: p. 716-719.
14. Hangai, Y., et al., *Functionally Graded Aluminum Foam Fabricated by Friction Powder Sintering Process with Traversing Tool.* Journal of Materials Engineering and Performance, 2016. **25**(9): p. 3691-3696.
15. Fang, T., et al., *Revealing extraordinary intrinsic tensile plasticity in gradient nano-grained copper.* Science, 2011. **331**(6024): p. 1587-1590.

16. Suresh, S., *Graded materials for resistance to contact deformation and damage.* Science, 2001. **292**(5526): p. 2447-2451.
17. Basu, S., Z. Wang, and C. Saldana. *Deformation heterogeneity and texture in surface severe plastic deformation of copper*. in *Proc. R. Soc. A*. 2016. The Royal Society.
18. Schoop, J., et al., *The effects of depth of cut and pre-cooling on surface porosity in cryogenic machining of porous tungsten.* Procedia CIRP, 2013. **8**: p. 357-362.
19. Jawahir, I., et al., *Cryogenic manufacturing processes.* CIRP Annals-Manufacturing Technology, 2016. **65**(2): p. 713-736.
20. Schoop, J., et al., *Cryogenic machining of porous tungsten for enhanced surface integrity.* Journal of Materials Processing Technology, 2016. **229**: p. 614-621.
21. Bram, M., et al., *Investigations on the machining of sintered titanium foams utilizing face milling and peripheral grinding.* Advanced Engineering Materials, 2003. **5**(6): p. 441-447.
22. Deglurkar, M., et al., *Evaluation of machining methods for trabecular metal implants in a rabbit intramedullary osseointegration model.* Journal of Biomedical Materials Research Part B: Applied Biomaterials, 2007. **80**(2): p. 528-540.
23. Teicher, U. and A. Nestler, *A method to simulate structural properties of cellular materials for machining processes.* Procedia CIRP, 2013. **8**: p. 100-104.
24. Fakhri, M.A., E. Bordatchev, and O. Tutunea-Fatan, *An image-based methodology to establish correlations between porosity and cutting force in micromilling of porous titanium foams.* The International Journal of Advanced Manufacturing Technology, 2012. **60**(9-12): p. 841-851.
25. De Chiffre, L., et al., *Industrial applications of computed tomography.* CIRP Annals-Manufacturing Technology, 2014. **63**(2): p. 655-677.
26. Dewulf, W., et al., *Uncertainty determination and quantification for dimensional measurements with industrial computed tomography.* CIRP Annals-Manufacturing Technology, 2013. **62**(1): p. 535-538.
27. Kruth, J.P., et al., *Computed tomography for dimensional metrology.* CIRP Annals-Manufacturing Technology, 2011. **60**(2): p. 821-842.
28. Bart-Smith, H., et al., *Compressive deformation and yielding mechanisms in cellular Al alloys determined using X-ray tomography and surface strain mapping.* Acta Materialia, 1998. **46**(10): p. 3583-3592.
29. Verhulp, E., B. van Rietbergen, and R. Huiskes, *A three-dimensional digital image correlation technique for strain measurements in microstructures.* Journal of biomechanics, 2004. **37**(9): p. 1313-1320.
30. Roux, S., et al., *Three-dimensional image correlation from X-ray computed tomography of solid foam.* Composites Part A: Applied science and manufacturing, 2008. **39**(8): p. 1253-1265.
31. McDonald, S., et al., *In situ three-dimensional X-ray microtomography of an*

auxetic foam under tension. Scripta Materialia, 2009. **60**(4): p. 232-235.
32. Singh, R., et al., *Characterization of the deformation behavior of intermediate porosity interconnected Ti foams using micro-computed tomography and direct finite element modeling.* Acta biomaterialia, 2010. **6**(6): p. 2342-2351.
33. Tutunea-Fatan, O., M. Fakhri, and E. Bordatchev, *Porosity and cutting forces: from macroscale to microscale machining correlations.* Proceedings of the Institution of Mechanical Engineers, Part B: Journal of Engineering Manufacture, 2011. **225**(5): p. 619-630.
34. Schoop, J., et al. *High performance infiltrant-free cryogenic machining of 82% density porous tungsten under computer numerical control*. in *Vacuum Electronics Conference, IEEE International*. 2014. IEEE.
35. Qiao, H., et al., *Subsurface damage in milling of lightweight open-cell aluminium foams.* CIRP Annals-Manufacturing Technology, 2017.
36. ASME B89.1.9-2002, *Gage Blocks*. American Society of Mechanical Engineers (ASME), 2002.
37. EN ISO 3650, *Geometrical Product Specifications (GPS)—Length standards—Gauge blocks ISO 3650:* 1998.
38. Kiekens, K., et al. *Parameter dependent thresholding for dimensional X-ray computed tomography*. in *Proceedings of the International Symposium on Digital Industrial Radiology and Computed Tomography*. 2011.
39. Canny, J., *A computational approach to edge detection.* IEEE Transactions on pattern analysis and machine intelligence, 1986(6): p. 679-698.
40. Ohtake, Y. and H. Suzuki, *Edge detection based multi-material interface extraction on industrial CT volumes.* Science China Information Sciences, 2013. **56**(9): p. 1-9.
41. Shakarji, C.M., *Least-squares fitting algorithms of the NIST algorithm testing system.* Journal of research of the National Institute of Standards and Technology, 1998. **103**(6): p. 633.
42. Meyer, F., *Topographic distance and watershed lines.* Signal processing, 1994. **38**(1): p. 113-125.
43. Jones, J.R., et al., *Non-destructive quantitative 3D analysis for the optimisation of tissue scaffolds.* Biomaterials, 2007. **28**(7): p. 1404-1413.
44. Gonzalez, R.C., *P. wintz digital image processing.* Addision-Wesley Publishing Company, 1987: p. 275-281.
45. Scarano, F., *Tomographic PIV: principles and practice.* Measurement Science and Technology, 2012. **24**(1): p. 012001.
46. Pan, B., D. Wu, and Z. Wang, *Internal displacement and strain measurement using digital volume correlation: a least-squares framework.* Measurement Science and Technology, 2012. **23**(4): p. 045002.
47. Germaneau, A., P. Doumalin, and J.-C. Dupré, *3D strain field measurement by correlation of volume images using scattered light: recording of images and choice of marks.* Strain, 2007. **43**(3): p. 207-218.
48. Pust, O. *Piv: Direct cross-correlation compared with fft-based cross-correlation*. in *Proceedings of the 10th International Symposium on*

Applications of Laser Techniques to Fluid Mechanics, Lisbon, Portugal. 2000.
49. McKenna, S. and W. McGillis, *Performance of digital image velocimetry processing techniques.* Experiments in fluids, 2002. **32**(1): p. 106-115.
50. Gates, M.R., *High performance digital volume correlation*. 2011: University of Illinois at Urbana-Champaign.
51. Gates, M., J. Lambros, and M.T. Heath, *Towards High Performance Digital Volume Correlation.* Experimental Mechanics, 2010. **51**(4): p. 491-507.
52. Lee, T.-C., R.L. Kashyap, and C.-N. Chu, *Building skeleton models via 3-D medial surface axis thinning algorithms.* CVGIP: Graphical Models and Image Processing, 1994. **56**(6): p. 462-478.
53. Inayat, A., et al., *Determining the specific surface area of ceramic foams: The tetrakaidecahedra model revisited.* Chemical Engineering Science, 2011. **66**(6): p. 1179-1188.
54. Warren, W. and A. Kraynik, *Linear elastic behavior of a low-density Kelvin foam with open cells.* TRANSACTIONS-AMERICAN SOCIETY OF MECHANICAL ENGINEERS JOURNAL OF APPLIED MECHANICS, 1997. **64**: p. 787-794.
55. Gibson, L.J. and M.F. Ashby, *Cellular solids: structure and properties*. 1999: Cambridge university press.